nature genetics

Supplementary information

https://doi.org/10.1038/s41588-025-02446-1

p53 inactivation drives breast cancer metastasis to the brain through SCD1 upregulation and increased fatty acid metabolism

In the format provided by the authors and unedited

Supplementary Information

Table of contents

Supplementary Notes 1-51

Supplementary Note 1

We observed a similar reduction in p53 pathway activity in immortalized human epithelial mammary (hTERT-HMEC) cells upon spontaneous acquisition of a heterozygous *TP53* mutation (**Extended Data Fig. 1f-h**). Subsequent spontaneous acquisition of del17p (or CRISPR-Cas9-based knockout of the functional *TP53* allele) resulted in further downregulation of the pathway (**Extended Data Fig. 1f-h**).

Supplementary Note 2

We note that a small, but significant, enrichment for biallelic inactivation of *TP53* was also observed in metastases to other organs (in comparison to primary tumors; $p=1*10^{-5}$; **Fig. 1c**), consistent with a general increased metastatic potential upon p53 loss[1]. However, the enrichment in BM was much greater (12% of primary tumors, 19% of non-BMs, and 50% of BMs).

Supplementary Note 3

We validated the transcriptional downregulation of the p53 pathway in BCBM using RNAseq data from a new clinical cohort of 6 BCBMs and 26 metastases from other organs (**Supplementary Fig. 1h** and **Supplementary Table 2**). We also performed RNAseq on 7 metastases obtained from an autopsy of a single BC patient. The transcriptional signature of the p53 pathway was indeed lower in the BM than in the other metastases (**Extended Data Fig. 1k**).

Supplementary Note 4

BM-specific downregulation of the p53 pathway was also observed in an independent cohort of 204 primary tumors from BC patients (**Extended Data Fig. 2b** and **Supplementary Table 3**)[2], as well as in a third cohort of 71 TNBC patients[3] with known metastatic sites (**Extended Data Fig. 2c**).

Supplementary Note 5

In all datasets (TCGA, METABRIC, MBC), BM-related signatures ranked highly among differentially-expressed signatures when comparing *TP53*-WT *vs*. *TP53*-perturbed tumors (**Supplementary Table 4**). We then correlated p53 pathway activity in primary breast tumors with transcriptional signatures associated with BM and found a highly significant negative correlation (**Extended Data Fig. 2f)**. We validated that these signatures were indeed increased in primary tumors that metastasized to the brain *vs*. those that metastasized to other organs (**Extended Data Fig. 2g** and **Supplementary Table 5**), and that they were independent of the specific mode (mut *vs* del) of p53 inactivation (**Extended Data Fig. 2h,i**). Importantly, *TP53* inactivation was negatively associated with bone-relapse transcriptional signatures (**Supplementary Fig. 3a-c**), indicating that the positive association was brain-specific. Similar

enrichments were observed when tumors with monoallelic and tumors with biallelic *TP53* inactivation were analyzed separately (**Supplementary Fig. 3d-j**), and also when each breast cancer molecular subtype was considered separately (**Supplementary Fig. 3k**).

Supplementary Note 6

We performed a pan-carcinoma analysis of the prevalence of *TP53* genetic alterations across primary tumors and metastatic sites in ~11,000 patients from the MSK-IMPACT dataset[4]. Both all and biallelic *TP53* genetic alterations were significantly more common in brain metastasis than in primary tumors and in other metastatic sites (**Extended Data Fig. 3b**).

Next, we analyzed the association between p53 inactivation and brain metastatic capacity across hundreds of human cancer cell lines **(Extended Data Fig. 3c**)[5]. A pan-carcinoma analysis revealed a significant enrichment for biallelic *TP53* inactivation in cell lines with high *vs.* low brain metastatic potential (**Extended Data Fig. 3d**). Furthermore, GSEA identified strong and significant downregulation of p53 pathway activity in cell lines with high *vs.* low brain metastatic potential (**Extended Data Fig. 3e** and **Supplementary Table 3**).

Supplementary Note 7

Across 23 human BC cell lines[5], *TP53* mutation was significantly associated with metastasis to the brain, but not to other organs (lung, liver, kidney, or bone), upon intra-cardiac injection (**Fig. 2a**). A comparison of the BC cell lines with high *vs.* low BM potential[5] (**Fig. 2b**) revealed that all (5/5) brain-metastasizing cell lines had a genetic alteration in *TP53* (**Fig. 2c**). GSEA of RNAseq data from these cell lines further confirmed a significant downregulation of the p53 pathway in the brain-metastasizing cell lines (**Fig. 2d** and **Supplementary Table 3**) and a significant upregulation of transcriptional signatures associated with brain-specific relapse (**Supplementary Fig. 3l-m**). We thus conclude that breast cancer cell lines recapitulate the clinical analysis and make for an appropriate system for functional and mechanistic studies.

Supplementary Note 8

Cells were fluorescently labeled, and *Trp53*/*TP53* was knocked-out using CRISPR-Cas9 to establish *Trp53*-null EMT6 / *TP53*-null CAL51 cell lines (**Supplementary Fig. 4a**). Sanger sequencing of the targeted locus confirmed the on-target disruption of *Trp53* (**Supplementary Fig. 4b**), qPCR confirmed that the mRNA levels of both *Trp53*/*TP53* and its transcriptional target *CDKN1A* (encoding for p21) were drastically reduced (**Supplementary Fig. 4c,d,f,g**), and Western blots showed that p53 protein levels were reduced to non-detectable levels in the knocked-out populations (**Supplementary Fig. 4e,h**).

Supplementary Note 9

We intra-cardially injected mCherry-labeled *Trp53*-WT cells and eGFP-labeled *Trp53*-null cells into the same mice and assessed their presence in the brain after 8 days (**Fig. 2j** and **Extended Data Fig. 4a**). In this experimental setup as well, *Trp53*-null cells gave rise to BM more frequently than *Trp53*-WT cells (**Extended Data Fig. 4b,c**), and the tumor burden and the number of metastatic foci were higher (**Fig. 2k** and **Extended Data Fig. 4d-j**). Importantly, no significant differences in the metastasis potential to the lung, liver or spleen were observed,

and there was a significant decrease in the metastatic potential to the bone (**Extended Data Fig. 4b-e**), consistent with our findings from patient data gene expression analysis **(Supplementary Fig. 3a-c, g-i)**.

Supplementary Note 10

TP53-null CAL51 cells gave rise to larger tumors (**Supplementary Fig. 6e,f)** and progressed faster than *TP53*-WT-derived tumors (**Supplementary Fig. 6g,h**). The same results were obtained with independently-generated CAL51 cells with *TP53* biallelic inactivation[6] (**Fig. 2o,p** and **Supplementary Fig. 6i-k**).

Supplementary Note 11

Astrocytes, the most abundant cell type of the brain, have been shown to enhance the survival, motility, and proliferation of metastatic cancer cells[7–14]. The increased astrocyte infiltration into *Trp53*-null tumors suggests that astrocytes might interact with BCBM cells in a p53-dependent manner.

Supplementary Note 12

We co-cultured the isogenic human cells with starvation-activated primary human astrocytes, and found that the human astrocytes indeed promoted cell proliferation in a p53-dependent manner (**Supplementary Fig. 7a**). Moreover, human ACM promoted cell proliferation of *TP53*-null cells significantly more than that of *TP53*-WT cells (**Supplementary Fig. 7b,c**), both when *TP53* was inactivated via biallelic knockout and when it was inactivated through hotspot mutations (relative to respective SFM controls; **Supplementary Fig. 7d-f**). In addition, astrocytes and ACM had a p53-dependent protective effect on cell viability: *TP53*-null cells exhibited improved survival and reduced cell death, as evaluated by live imaging and by flow cytometry using Sytox green and Annexin-V staining (**Supplementary Fig. 7g-k**).

Similar to our observations with the mouse cells, *TP53*-null CAL51 cells exhibited higher migration capacity in the presence of astrocytes or ACM in comparison to *TP53*-WT cells (**Supplementary Fig. 7l-r**). Live cell imaging-based single-cell tracking also revealed that ACM preferentially increased the motility of *TP53*-null cells (**Supplementary Fig. 7p -r**).

Supplementary Note 13

High metastatic capacity to the brain was associated with elevated lipid metabolism across human BC cell lines (**Fig. 4c** and **Supplementary Table 7 and 10**), and the same pathways were also transcriptionally upregulated upon *TP53* loss in CAL51 cells (**Fig. 4d** and **Supplementary Table 7**). In line with these results, elevated lipid metabolism was also observed upon the spontaneous acquisition of a *TP53* mutation in hTERT-HMEC cells (**Extended Data Fig. 6f**).

Supplementary Note 14

We also found a significant increase in palmitic acid and oleic acid (OA; 18:1)-containing triglycerides in ACM (**Fig. 4e**, **Extended Data Fig. 6g** and **Supplementary Table 13**).

Supplementary Note 15

CD36 mRNA and protein levels were already elevated in *Trp53*-null *vs. Trp53*-WT EMT6 cells under SFM conditions (**Fig. 4o,q**). Importantly, CD36 levels were further upregulated when cells were cultured in ACM, and this upregulation was much more pronounced in *Trp53*-null cells (relative to SFM **Fig. 4p-r**). A similar preferential upregulation of CD36 was observed in ACM-cultured *TP53*-null *vs. TP53*-WT human CAL51 cells (**Extended Data Fig. 6k,l**).

Supplementary Note 16

Indeed, BM sections that contained extensive astrocyte infiltration exhibited more CD36-positive cells and higher CD36 protein levels than samples with no infiltration **(Fig. 4w,x, Supplementary Fig. 9** and **Supplementary Table 6)**. A cell proximity analysis by confocal microscopy confirmed that CD36-positive cells were on average significantly closer to GFAP+ astrocytes than CD36-negative cells in BCBM (**Fig. 4y,z**).

Supplementary Note 17

FASN mRNA levels were elevated in *TP53*-null *vs. TP53*-WT primary BCs (Luminal B subtype, for TCGA and METABRIC datasets **Extended Data Fig. 7f-h)**, and a significant negative correlation was observed between *FASN* expression and p53 pathway activity (**Extended Data Fig. 7i**).

Supplementary Note 18

SCD1 and FASN were elevated in *TP53*-null *vs. TP53*-WT human CAL51 cells, and ACM further increased their expression levels (**Supplementary Fig. 10 a-f**). CAL51 cells with hotspot *TP53* mutations R175H and R273H also increased their SCD1 and FASN expression following ACM exposure (**Extended Data Fig. 7l-o**).

Supplementary Note 19

Recent studies suggest that brain metastatic cells are metabolically flexible, and especially when oxygen supply is low, the use of glucose for FAS is limited and additional carbon sources are required[15–18]. Glutamate and glutamine levels, in contrast, are high in the brain, and have been shown to be utilized for FAS in both brain and cancer cells[15,16,19].

We found elevated *HIF1A* levels and expression signatures of hypoxia in p53-deficient breast carcinomas, as well as in our p53-null isogenic cells (**Supplementary Fig. 12 a-d**), consistent with the known association between p53 inactivation and hypoxia[20].

Supplementary Note 20

Importantly, glutamate supplementation led to a significant increase of SCD1 and FASN protein levels, specifically in the *Trp53*-null cells (**Extended Data Fig. 8j-l**), indicating that p53 inactivation increased the ability and/or need of the cancer cells to utilize glutamate for FAS.

Supplementary Note 21

In contrast to the increased labeling of FAs with ^{13}C-glutamate, no differential FA labeling was observed between *Trp53*-WT and *Trp53*-null BC cells following incubation with ^{13}C-glucose, (**Extended Data Fig. 8o**).

Analysis of polar metabolites further revealed a shift toward increased utilization of the reductive carboxylation pathway (reverse TCA) in *Trp53*-null cells, consistent with elevated FAS from glutamate in these cells (**Supplementary Fig. 12 e,f** and **Supplementary Table 15**).

Supplementary Note 22

More generally, we noted a significant overlap between p53-bound and SREBP1-bound genes (14% overlap with SREBP1, ChIP atlas data, **Extended Data Fig. 9c** and **Supplementary Table16**).

Supplementary Note 23

Of importance, SREBP1 is known to be a direct transcriptional regulator of SCD1[21], and p53 was previously shown to regulate SREBP1 in adipose tissue[22]. In line with our CUT&Tag results, *TP53*-null CAL51 cells showed increased levels of *SREBP1* mRNA levels (**Extended Data Fig. 9d**).

Supplementary Note 24

DEPDC1 mRNA levels were increased in TCGA breast tumors with *TP53* alterations (**Fig. 6g** and **Extended Data Fig. 9h**). Importantly, *DEPDC1* mRNA levels were negatively correlated with p53 pathway activity in primary breast tumors (**Fig. 6h**). We then compared breast tumors with high (top 10%) *DEPDC1* expression to tumors with low (bottom 10%) *DEPDC1* expression by GSEA and found downregulation of p53 targets in *DEPDC1*-high tumors (**Extended Data Fig. 9i**).

Supplementary Note 25

Comparison of high- *vs.* low-*DEPDC1* expressing tumors revealed a similar enrichment of lipid metabolism signatures in tumors that express high levels of *DEPDC1* ('Burton_Adipogenesis-3' ranked 13 out of 5,844 signatures **Extended Data Fig. 9j**). siRNA-mediated knockdown of *DEPDC1* in four breast cancer cell lines (*TP53*-WT, *TP53*-mut/mut and *TP53*-mut/del17p) strongly reduced SCD1 expression in all cell lines (**Fig. 6k-m** and

Extended Data Fig. 9k-m). Further, high *DEPDC1* mRNA levels were significantly associated with high *SCD1* mRNA levels in breast carcinomas (**Fig. 6n**).

Supplementary Note 26

DEPDC1 was reported to bind a ZNF transcription factor to regulate transcription and oncogenicity in bladder cancer cells[23]. We therefore tested whether DEPDC1 directly binds *SCD1* regulatory sequences using chromatin immunoprecipitation (ChIP). Both endogenous and HA-tagged DEPDC1 showed a two-fold binding enrichment of DEPDC1 over IgG control at the proximal promoter of the SCD1 gene, directly upstream of the transcriptional start site (Region C) (**Fig. 6o** and **Extended Data Fig. 9n**). This enrichment was specific to this site, as no binding was detected at three other regulatory regions tested (Region A,B, intron1).

Supplementary Note 27

The DEPDC1-bound site contains a polyunsaturated fatty acid (PUFA) response element that is bound by SREBPs. As SREBP1 binding is known to bind to the same region of the SCD1 promoter[75], we hypothesized that DEPDC1 might regulate *SCD1* transcription via interaction(s) with SREBP1. In line with this notion, GSEA comparison of high- *vs.* low-*DEPDC1* expressing breast tumors showed increased SREBP target gene expression, including *SCD1*, in *DEPDC1*-high tumors (**Extended Data Fig. 9o,p**). We therefore performed reciprocal immunoprecipitations (co-IPs) to assess the protein-protein interaction between DEPDC1 and SREBP1. Indeed, immuno-precipitates from endogenous DEPDC1 pulled down SREBP1, and *vice versa* (**Fig. 6p**), indicating a protein-protein interaction between the two.

Supplementary Note 28

We evaluated whether ACM would affect *Srebp1* and *Depdc1* expression in our *p53*-WT/*p*53-null isogenic breast cancer cells. ACM exposure significantly increased both *Srebp1* and *Depdc1* transcript levels in *Trp53*-null *vs. Trp53*-WT cells (**Fig. 6s** and **Extended Data Fig. 9s**), similar to the results obtained for SCD1 (**Fig. 5d-f).** DEPDC1 protein levels were similarly higher in *Trp53*-null *vs. Trp53*-WT cells cultured in ACM (relative to their SFM controls; **Fig. 6t,u**). A similar elevation was observed in the *TP53*-null *vs. TP53*-WT human CAL51 cells (**Extended Data Fig. 9t-v**).

Supplementary Note 29

TP53-null human BC cell lines were significantly more sensitive than *TP53*-WT cell lines to genetic (RNAi-mediated) knockdown and to pharmacological inhibition (with the drug C75) of FASN (**Extended Data Fig. 10i,j**). Consistently, the isogenic *Trp53*-null cells were significantly more sensitive to the FASN inhibitor, C75, and to the SREBP1 inhibitor Fatostatin, than *Trp53*-WT cells (**Fig. 7e** and **Extended Data Fig. 10k-m, Supplementary Fig. 15 d).** Finally, *Trp53*-null cells were also more sensitive to the CD36 inhibitor SSO (**Supplementary Fig. 15 e,f**).

Supplementary Note 30

We performed bi-lateral intra-cranial injections of *Trp53*-WT and *Trp53*-null EMT6 BC cells into immunocompetent mice, allowing us to compare tumors that differ in their p53 status within the same brain (**Fig. 7h**). The following day, we started injecting mice twice daily either with the SCD1 inhibitor SW203669 (intraperitoneal 40mg/kg) or with vehicle (10% Kolliphor). We then assessed tumor growth over 11 days by MRI imaging. After 11 days, *Trp53*-null tumors (vehicle injected) were larger than WT controls (1.6-fold difference **Fig. 7i,j**), similar to our results presented in **Fig. 2n**. Importantly, *Trp53*-null tumors exposed to SCD1i were significantly smaller than *Trp53*-null tumors injected with vehicle, and were also significantly smaller than *Trp53*-WT tumors treated with SCD1i (72% reduction of tumors size in *Trp53*-null (SCD1i) *vs Trp53*-null (vehicle), 75% reduction in *Trp53*-null (SCD1i) *vs Trp53*-WT (SCD1i) **Fig. 7i,j**). In fact, whereas tumor size started declining in SCD1i-treated *Trp53*-null tumors around day 7, vehicle-treated tumors – as well as SCD1i-treated *TP53*-WT tumors, continued to grow (**Fig. 7k**)

Supplementary Note 31

TP53 is the most studied gene in human cancer[24]. Why has the overwhelmingly strong association between p53 inactivation and BCBM been previously overlooked? One reason might be that in recent years, most of the focus has been on matched analyses of primary tumors and their derived metastases[64,86]. Such analyses make for a clean system to study genomic alterations that arise during metastasis, but they would inevitably miss common drivers that pre-exist in the primary tumors. In the case of p53, we reveal that its status in the primary BC lesion is already strongly associated with the risk for BCBM, so this association would not come up in matched analyses. A second reason is that p53 inactivation is often achieved through loss of the entire chromosome arm (del17p). Aneuploidy is commonly ignored in genomic analyses of metastases, and when del17p is overlooked, the link between p53 inactivation and BCBM becomes much weaker[25]. In contrast, when aneuploidy status is integrated into the analysis, the association between p53 perturbation and BCBM becomes strong and significant (**Fig. 1a-d, Supplementary Fig. 1b**). Therefore, our study emphasizes the importance of integrating aneuploidy calls into cancer genomic analyses.

Supplementary Note 32

Previous studies have begun to reveal the importance of metabolic adaptations – and of lipid metabolic adaptations in particular – in metastasis[26–29]. Our finding that BCBM cells upregulate both FA synthesis and uptake (**Fig. 7o**) is intriguing, as they seem to be redundant mechanisms. However, our data suggest that both CD36 and SCD1 p53-dependent upregulation serve the same purpose – MUFA synthesis – which is essential for BCBM. Nonetheless, whether there is functional redundancy between FA synthesis and uptake in BCBM, and whether this redundancy could contribute to drug resistance[5,30–33] remain open questions. It is also reasonable to speculate that other lipids, such as cholesterol – whose biosynthesis is known to be regulated by p53[34–36] – might also promote BCBM in a p53-dependent manner. Particularly, as both MUFAs and cholesterol are needed to generate cholesterol esters required for membranes and proliferation.

Supplementary Note 33

Does del17p affect BCBM through additional, p53-independent mechanisms? Glioblastomas commonly inactivate p53[37], and have been recently shown to depend on FAS[38–42], suggesting that our findings may be relevant to primary brain tumors as well.

Does p53 inactivation contribute to BCBM through additional mechanisms? Likely mechanisms include altered chemokine signaling[8,43–45], as well as the regulation of matrix metalloproteinases (MMPs)[1,46] and Serpins[47–49], which have been previously implicated in BM and also been shown to be regulated by p53[1]. Another potential mechanism is mTOR signaling[50–55], which is upstream of FAS[55], is responsive to amino acids such as glutamate[56], and has been implicated in BM. It is thus tempting to speculate that astrocytes may affect the activity of the mTOR pathway in BCBM in a p53-dependent manner. Notably, several of these mechanisms are clinically targetable.

Does del17p affect BCBM through additional, p53-independent mechanisms? We report the loss of chromosome 17p, to be extremely common in BCBM. While it is clear from our results that p53 inactivation is a consequential outcome of del17p, this large-scale chromosome-arm loss may affect BCBM through additional, p53-independent mechanisms; whether such mechanisms exist – and might be targeted – remains unknown.

Do other aneuploidies affect metastatic organotropism in BC and in other cancer types? We have found that aneuploidy-driven perturbation of a tumor suppressor gene could have a profound impact on metastatic organotropism. It will be important to further explore the role of aneuploidy in determining metastatic organotropism in BC and in other cancer types.

Supplementary Note 34

The identification of patients with elevated risk for BCBM based on the p53 status of their primary tumors, could affect patient care in at least two ways:
(a) This particular subset of patients may specifically benefit from frequent head MRI scans – a medical procedure not routinely offered to BC patients in most healthcare systems.
(b) For patients with tumors of the HER2-enriched molecular subtype, several existing targeted therapies differ both in their ability to penetrate the blood-brain barrier (BBB) and in their overall toxicity[57]; for example, the small molecule tyrosine kinase inhibitor, Neratinib, (as opposed to anti-HER2 antibodies) penetrates relatively well to the brain but is associated with a relatively high toxicity[58]. This drug should therefore be targeted at patients with high BCBM risk, whereas drugs with lower toxicity and lower brain penetration might be a better treatment for patients with low BCBM risk

Supplementary Note 35

Cell culture. MDA-MB-231, MDA-MB-468, SK-BR-3 were cultured in DMEM (Lonza) + 10% FBS (Euroclone); MCF7 in EMEM + FBS, NEAA, insulin (10 μg/ml); MCF10A in DMEM/F12 + 5% horse serum, EGF (20 ng/ml), insulin (10 μg/ml), hydrocortisone (500 ng/ml); 4T1 in RPMI + 10% FBS. All media contained penicillin (100 U/ml) and streptomycin (10 μg/ml). Human (ScienceCell #1800) and murine astrocytes were cultured in astrocyte medium (ScienceCell #1801) + 2% FBS, 1% supplements, and not propagated >P5. All cultures were mycoplasma-free.

Supplementary Note 36

Delipidation of cell culture medium. 0.1-0.5g of fumed silica (Sigma) was added to the cell culture medium, rotated for 2hrs and then centrifuged at 3000xg for 35min at RT. The supernatant was filtered through a 0.45µm and a 0.22µm filter.

Supplementary Note 37

Fluorescent labeling of BC cell lines. For green fluorescence, eGFP (pLEX_TRC206) was packaged in a 3rd generation lentiviral system. Briefly, 293T cells were transfected with 1µg lentiviral vector and packaging plasmids (pMDLg/pRRE 0.65µg, pRSV.Rev 0.25µg, pMD.G 0.35µg) using JetPEI (Polyplus #101-10N). Medium was replaced the following morning, and lentivirus-containing supernatant was collected at 48 and 72hrs, filtered (0.45µm), and used to infect target cells with 8µg/mL polybrene (Sigma #TR-1003-G). Medium was replaced the next day, cells were expanded for two passages, and eGFP-positive cells were isolated by FACS.

Supplementary Note 38

Cell death analysis. Cells were washed twice with cell staining buffer (BioLegend #420201), resuspended in binding buffer (BioLegend #422201), and incubated with 2.5µL AnnexinV (BioLegend #640920, 12µg/mL) and 1µL PI (BioLegend #421301, 0.5mg/mL) for 15min at room temperature in the dark. CAL51 cells were similarly treated for 72hrs and stained with Sytox Green (Invitrogen S34860, 1:1000) and Pacific Blue–AnnexinV (BioLegend #640918, 60µg/mL) for 15min at room temperature. Data was acquired on a CytoFLEX flow cytometer (Beckman Coulter) and analyzed with CytExpert 2.4 software. For live-cell imaging of cell death, Sytox™ dead cell stain (Invitrogen S34860, 1:10,000) was used as described above. FACS gating strategies in **Supplementary Fig.16**.

Supplementary Note 39

MRI. Mice were scanned using conventional T1 or T2 protocols on 4.7T or 7T MRI systems (MR Solutions, UK) with a 32-channel head coil, following intraperitoneal gadolinium injection (Soreq, Israel). T1 images were analyzed using RadiAnt DICOM Viewer or MRIcro. Tumor area was measured on each axial slice, and total tumor volume was calculated by summing all slice areas.

Supplementary Note 40

RNA extraction. Cell pellets were incubated in 100µL Bio-TRI® (Bio-Lab) at −80°C for 1hr, followed by chloroform (1:5), vortexing, 3min at room temperature, and centrifugation at 12,000xg, 4°C for 15min. The aqueous phase was mixed with 100µL isopropanol and 1µL glycogen (Thermo Fisher R0561), incubated overnight at −20°C, then RNA was pelleted, washed, and resuspended in DEPC-treated water.

Supplementary Note 41

RNA sequencing after *DEPDC1* knockdown. Total RNA was extracted using RNeasy Mini Kit (Qiagen 74104) with DNase treatment (Qiagen 79254). mRNA libraries were prepared using Illumina TruSeq Stranded mRNA Kit and sequenced on Illumina NovaSeq 6000 (100 bp paired-end, 60M reads).

FASTQ files were quality-checked with FastQC and aligned to GRCh38 using STAR to generate raw counts. Differential expression was analyzed with DESeq2. Gene set enrichment

analysis (GSEA) was performed using the REACTOME dataset (fgsea package) with significance thresholds of adjusted q-value < 0.05 and NES > 1 or NES < −1. Analyses were performed in R/Bioconductor. Data are available at GEO (GSE281411).

Supplementary Note 42

RNA sequencing of HMEC cells. Cells were lysed, and total RNA was purified using Qiagen RNeasy Plus Kit (#74134). Two µg RNA per sample underwent mRNA purification (NEBNext Poly(A) mRNA Magnetic Isolation Module #E7490L) and library preparation using NEBNext Ultra II Directional RNA Library Prep Kit (#E7765L) with NEBNext Multiplex Oligos (#E6440S). Libraries were quantified by qPCR (NEBNext Library Quant Kit #E7630S), multiplexed, and sequenced single-end on NextSeq2000 (Illumina, P2 XLEAP-SBS 100 cycle).

FASTQ files were generated using BCL Convert v3.8.2, aligned to hg19 with BWA v0.7.17[63], and sorted using Samtools v1.16.1[64]. Gene-level counts were obtained with featureCounts v1.6.2[65], converted to RPKM, and differential expression was analyzed using edgeR v3.36.0[66]. Gene set enrichment analysis (GSEA) was performed with fgsea v1.20.0[67] using MSigDB[68,69] and custom gene sets, including a nutlin response (p53 activation) set[70], on pre-ranked gene lists weighted by $\log_2$(fold change) with 10,000 permutations.

Supplementary Note 43

RNA sequencing of patient tumor samples. RNA was extracted using the AllPrep DNA/RNA/miRNA Universal Kit (Qiagen). RNA quality was assessed by Bioanalyzer (Agilent RNA 6000 Nano Kit). Libraries were prepared using TruSeq RNA Exome Kit (Illumina), quality-checked by Bioanalyzer (High Sensitivity DNA Kit), quantified by qPCR, and sequenced paired-end (76 bp) on NextSeq 500. Data were processed with the nf-core "rnaseq" v3.9 pipeline using STAR for alignment and Salmon for gene quantification with default parameters.

Supplementary Note 44

RNA sequencing of patient autopsy samples. mRNA was extracted using the miRNeasy Kit (Qiagen #217084) Genomic DNA was removed with RNase-Free DNase (Qiagen #79254). RNA quality and quantity were assessed using Agilent 4200 TapeStation, and 100 ng mRNA per sample was used for library preparation with TruSeq RNA Library Prep Kit (Illumina). Libraries were pooled, diluted to 1.5 pM, and sequenced paired-end (2 × 81 cycles) on NextSeq 500 (Illumina, v2 150 cycle high-output kit).

Reads were aligned to GRCh38 using Subread aligner[71], and gene counts were generated with featureCounts[65] for NCBI RefSeq genes. Genes with CPM <1 in all libraries or lacking official symbols were excluded. Counts were transformed to log2-CPM, quantile-normalized using the voom function (limma)[72,73], and further converted to log2-RPKM.

Supplementary Note 45

Fatty acid content analysis. Lipid samples from 5 ml medium or cell pellets (corresponding to $2*10^6$ cells) were transferred into a screw-capped tube (teflon-lined) containing 5µg heptadecanoic acid as internal standard. 1ml B3F in methanol was added for FA esterification. The tubes were gassed with nitrogen and heated at 90ºC for 45 min with occasional shaking. After cooling, 1ml hexane was added, the mixture was centrifuged briefly, and the hexane layer

containing fatty acid methyl ester (FAME) derivatives was transferred to a fresh tube. Hexane extracts were concentrated under nitrogen, and 1 µl of a one-twentieth dilution in hexane was applied to a gas chromatograph. FAs were analyzed as FAME derivatives by gas chromatography using a Varian 3800 Series chromatograph with flame ionization detection (FID) and a fused silica SGE capillary column (30 × 0.025 mm), using Varian Star Workstation Advance Application software version 6.x. FA profiles were identified by comparison with a known mixture (PUFA2, Supelco, USA) and quantified relative to the internal standard[74].

Supplementary Note 46

100µL of medium samples (SFM or ACM) were mixed with 1mL of cold (−20°C) methanol: methyl-tert-butyl-ether (MTBE, 1:3, v/v) containing internal standards: phosphatidylcholine (17:0/17:0, 0.1µg/mL), phosphatidylethanolamine (17:0/17:0, 0.4µg/mL), ceramide/sphingoid internal standard mixture II (0.1 nmol/mL), d5-TG internal standard mixture I (0.0267µg/mL), and ^{13}C-palmitic acid (0.1 µg/mL). Samples were vortexed, sonicated for 30min on ice with brief vortexing every 10min, and then 0.5mL of water:methanol (3:1, v/v) containing ^{13}C/^{15}N-labeled amino acids was added. Tubes were vortexed and centrifuged; the upper organic phase was collected. The polar phase was re-extracted with 0.5mL MTBE, and organic phases were combined, dried under vacuum, and stored at −80°C. Polar metabolites were dried similarly.

For lipidomics, dried extracts were resuspended in 250µL mobile phase B, centrifuged at 19,000 ×g, 4°C, and 225µL transferred to HPLC vials. Analyses were performed on a Waters ACQUITY UPLC I-class system coupled to a Thermo Exactive Plus Orbitrap MS in switching positive/negative ionization mode[152]. Separation used an ACQUITY UPLC BEH C8 column (2.1× 100 mm, 1.7µm) at 40°C, 0.4 mL/min flow rate. Mobile phases: A = DDW:ACN:IPA (46:38:16) + 1% 1M NH4Ac, 0.1% acetic acid; B = DDW:ACN:IPA (1:69:30) + 1% 1 M NH4Ac, 0.1% acetic acid. Gradient: 100% A for 1min, linear to 25% A at 12 min, to 0% at 16 min, 100% B to 21 min, then 100% A for column equilibration to 25 min. Lipids were identified and quantified with LipidSearch™ software and validated against an in-house library; relative levels were normalized to internal standards and protein content.

For polar metabolites, dried extracts were resuspended in 100µL methanol:DDW (50:50), centrifuged, and 60µL injected into HPLC vials. Separation used a SeQuant Zic-pHILIC column (150×2mm) with guard column (20×2.1mm) at 200µL/min. Mobile phase A = 20mM ammonium carbonate + 0.1% ammonia hydroxide in water:ACN (80:20); B = ACN. Gradient: 0–2min, 75% B; 2–14min, 25% B; 14–18 min, 25% B; 18–19 min, 75% B; 19–23 min, 75% B. MS data were acquired in negative mode. Metabolites were identified using Progenesis QI based on accurate mass, retention time, isotope pattern, fragmentation, and verified against an in-house mass spectra library.

Supplementary Note 47

^{13}C-Isotope tracing. Sample preparation for FA analysis: After labeling, cells were washed twice with ice-cold saline and extracted with 60% methanol containing 5µM L-norleucine as internal standard. Samples were lyophilized and subjected to fatty acid methyl ester (FAME) derivatization with 100µL toluene, 750µL methanol, and 150µL 8% HCl in methanol at 100°C for 1hr with shaking (ThermoMixer C, Eppendorf). After cooling, samples were dried under N_2, re-dissolved in 100µL hexane, and 1–2µL were injected for GC-MS analysis. GC-MS of labeled fatty acids: Analysis was performed using a 7890B GC system coupled to a 7250 GC/QTOF mass spectrometer with PAL RSI 85 autosampler. Separation was achieved on an HP-5MS column (30 m × 0.25mm × 0.25µm) at 1.2mL/min constant flow, using the following

gradient: 2min at 80°C, ramp 15°C/min to 320°C, hold 6min. Injection was splitless at 230°C, transfer line at 280°C, source at 200°C, detection range 50–500 amu. FAME 37-component standard mix (CRM47885, Supelco) was used for peak assignment. Characteristic m/z values for isotopologues were: palmitoleic acid methyl ester 236.2134–252.2671, palmitic acid methyl ester 270.2558–286.3095, oleic acid methyl ester 296.2715–314.3319, stearic acid methyl ester 298.2870–316.3474. Phase separation for polar fraction analysis: For samples incubated with ^{13}C-glutamic acid or ^{13}C-glucose, chloroform was added (1:1 v/v) with linoleic acid-d32 as an internal standard, followed by 15min sonication and 15min centrifugation at 21,000 ×g, 4°C. Lipophilic fractions were dried and processed as above; polar fractions were dried for derivatization. GC-MS of polar metabolites: Dried polar fractions were treated with 40µL methoxyamine hydrochloride (20 mg/mL in pyridine) at 37°C for 90min, followed by 70µL N,O-bis(trimethylsilyl)trifluoroacetamide at 37°C for 30min. Analysis was performed on a 7820AN GC coupled with a 5975 MS (Agilent) using HP-5ms column (30 m × 250 µm × 0.25 µm), helium flow 1mL/min, and a temperature program: 70–150°C at 4°C/min, 150–215°C at 9°C/min, 215–300°C at 25°C/min, hold 5 min. MS was operated in electron impact full-scan mode (m/z 30–500), inlet 280°C, transfer line 280°C, ion source 250°C. Injection (1µL) was splitless. Data analysis: Isotopologue peak areas were acquired using Agilent Mass Hunter workstation software. IsoCor[75]was used to correct for natural isotope abundance and calculate mean ^{13}C enrichment.

Supplementary Note 48

Chromatin immunoprecipitation. MDA-MB-231 cells were cross-linked with 1%formaldehyde for 15min, neutralized with 125mM glycine (pH 2.5), and washed with PBS. Cells were scraped in PBS containing protease inhibitors (Sigma) and 1mM PMSF, then centrifuged at 1,700 × g for 10min at 4°C. Cell pellets were lysed in buffer containing 50mM Tris-HCl (pH 8.1), 1% SDS, 10mM EDTA, protease inhibitor cocktail, 1mM PMSF, and 5mM NaF. Nuclei were pelleted, washed in 10mM Tris-HCl (pH 7.5), 200mM NaCl, 1mM EDTA, and resuspended in shearing buffer (0.1% SDS, 1 mM EDTA, 10 mM Tris-HCl, pH 7.5). Chromatin was sonicated using a Bioruptor sonicator (Diagenode, medium power) for 30min to yield fragments of ~250–300bp, centrifuged at 18,000 × g for 10min at 4 °C, and supernatants were diluted 2-fold in ChIP dilution buffer (0.01% SDS, 1% Triton X-100, 2mM EDTA, 20mM Tris-HCl pH 8.1, 500mM NaCl). Chromatin was pre-cleared with Protein A/G PLUS-Agarose beads (Santa Cruz Biotechnology) for 1hr at 4°C, and 10% of each sample was reserved as input. Immunoprecipitation was performed overnight at 4 °C using 1µg of DEPDC1 antibody or anti-HA Y11 (Santa Cruz Biotechnology, sc-805). DNA–protein complexes were captured with Protein A/G PLUS-Agarose and washed sequentially with 1ml of low-salt wash buffer (0.1% SDS, 1% Triton X-100, 2 mM EDTA, 20 mM Tris-HCl pH 8.1, 150 mM NaCl), high-salt wash buffer (0.1% SDS, 1% Triton X-100, 2 mM EDTA, 20 mM Tris-HCl pH 8.1, 500 mM NaCl), LiCl wash buffer (250 mM LiCl, 1% NP-40, 1% deoxycholate, 1mM EDTA, 10mM Tris-HCl pH 8.1), and finally TE buffer. Samples were treated with RNase in TE for 30min at 37 °C. Protein–DNA complexes were eluted in 1% SDS/0.1 M $NaHCO_3$, vortexed, incubated for 15min at room temperature, and pelleted. Eluates were combined with 20µl of 5M NaCl and de-crosslinked overnight at 65°C. Inputs were processed in parallel. DNA was purified by phenol/chloroform extraction and ethanol precipitation, then resuspended in H_2O. qPCR was performed using iTaq Universal SYBR Green Supermix (Bio-Rad). Promoter occupancy was calculated as fold enrichment of immunoprecipitated chromatin over control IgG using the 2^–ΔCt method.

Supplementary Note 49

***In vitro* drug treatments and metabolite supplementation.** The following chemicals and dilutions were used: **Nutlin-3** (#S1061, Cayman), 10 μM for 24 hrs. **SCD1 inhibitor** SW203668140 (#19379, Cayman), 0.1–3μM, with daily replacement for 3days. SCD1 inhibitor A939572 (#1939572, Cayman), 75μM. **FASN inhibitor** C75 (#10005270, Cayman), 3–100μM for 3 days. **SREBP1 inhibitor** Fatostatin (#13562, Cayman), 1.25–10μM for 5days. **CD36 inhibitor** SSO (#11211, Cayman), 10–160μM for 3days. **Palmitic acid** (PA, #P9767, Sigma) and **palmitoleic acid** (POA, #P9417, Sigma), dissolved in methanol and DMSO, respectively, in DMEM with 0.5mM glutamine and 1% FBS. **Oleic acid** (OA, #90260, Cayman), 2.5–50μM. **Glutamate** (G1626-100G, Sigma), 75mM in glutamine-free astrocyte medium (ScienCell; 1801-NG). For SCD1 inhibitor rescue experiments, cells were cultured in AM-NG medium supplemented with 0.5% glutamine and 1% FBS.

Supplementary Note 50

SCD1 inhibitor treatment of human BM organotypic cultures. Resected human BMs were collected in HBSS (Sigma Aldrich, 55037C) on ice, dissected into small pieces and embedded in 4% low-melting agarose (Sigma Aldrich, A9414). Embedded tissue pieces were sectioned into 250 μm slices using a vibratome (Leica, VT1200 S) and maintained in ice-cold HBSS until culture. BM slices were cultured on floating membranes (Whatman, 10417301) in brain slice medium[160] with either vehicle (DMSO; Sigma Aldrich, D8418) or SCD1 inhibitor (SW203668, 3μM; Sigma Aldrich, SML1702) for 3 days. Vehicle and SCD1 inhibitor were refreshed every 24hrs. Slices were then fixed in 4% PFA (Roth, P087) for 24hrs at room temperature prior to FFPE processing.

From FFPE tissue blocks, 3 μm sections were cut and stained with H&E or subjected to immunohistochemistry (IHC) using an automated platform (Ventana BenchMark AutoStainer, Ventana Medical Systems, Tucson, AZ, USA). Sections were baked overnight at 60 °C and deparaffinized with EZ Prep Concentrate solution (Ventana Medical Systems, AZ, USA). Antigen retrieval was performed with ULTRA Cell Conditioning solution (ULTRA CC1, pH 8.5; Ventana Medical Systems) at 95 °C. Primary antibodies used included anti-Ki67 (Clone 30-9), anti-Cleaved Caspase-3 (CST, #9661), anti-SCD1 (Abcam, ab19862), anti-p53 (clone DCS-60.2), and anti-p21WAF1 (clone DCS-60.2). UltraView Universal DAB Detection kit was used for Ki67, cleaved Caspase-3, p53, and p21; OptiView DAB IHC Detection and OptiView Amplification kits were used for SCD1. A universal HRP multimer was applied as the secondary antibody cocktail, and sections were counterstained with Hematoxylin and Bluing reagent (Ventana Medical Systems, AZ, USA).

IHC quantification was performed independently by two researchers. Validation was carried out using QuPath software v0.5.1[76]. The "Positive cell detection" analysis was applied to the entire section, excluding non-tumoral areas, to determine the total number of positive cells for each marker. Antibody details are provided in **Supplementary Table 19**.

Supplementary Note 51

Details of each statistical test, the number of analyzed samples and the number of independent experiments are specified in the Figure legends. Significance is indicated as: *,$p<0.05$, **,$p<0.01$, *** ,$p<0.001$, ****,$p<1*10^{-4}$.

Comparisons between two groups were performed using two-sided or one-sided Student's *t*-tests as appropriate. Paired Student's *t*-tests were applied for patient-matched expression analyses and bilateral intracranial injections containing matched p53-WT and p53-null cells. When one or both groups showed non-normal data distributions, the Mann–Whitney test (independent samples) or Wilcoxon signed-rank test (paired samples) was used. Two-way ANOVA was applied to determine significance for interventions in mice comparing p53-WT and p53-null groups. Two-sided Chi-square tests or Fisher's Exact tests (for small sample sizes) were used to assess differences in event prevalence between groups.

Significance of GSEA was determined based on the normalized enrichment score (NES) and false discovery rate (FDR q-value) calculated using GSEA software (version 4.03). Significance of ssGSEA was assessed using two-sided or one-sided Student's *t*-tests, with Q-values computed using the Benjamini–Hochberg method.

IC_{50} values were calculated using the "concentration versus normalized response, 4 parameters (variable slope)" equation in GraphPad PRISM 9.1. Correlations and linear regressions were also calculated using GraphPad PRISM 9.1. Survival curves were generated using the Kaplan–Meier method, with significance determined by the Gehan–Breslow–Wilcoxon test, which emphasizes early events. One-sided tests were generally used when the experimental direction was predicted based on prior results from a different dataset or cell line.

In all presented box plots, individual data points are shown. The internal line represents the median, the box spans the 25th to 75th percentiles, and whiskers extend to the highest and lowest data points.

Supplementary Figures

Supplementary Fig.1

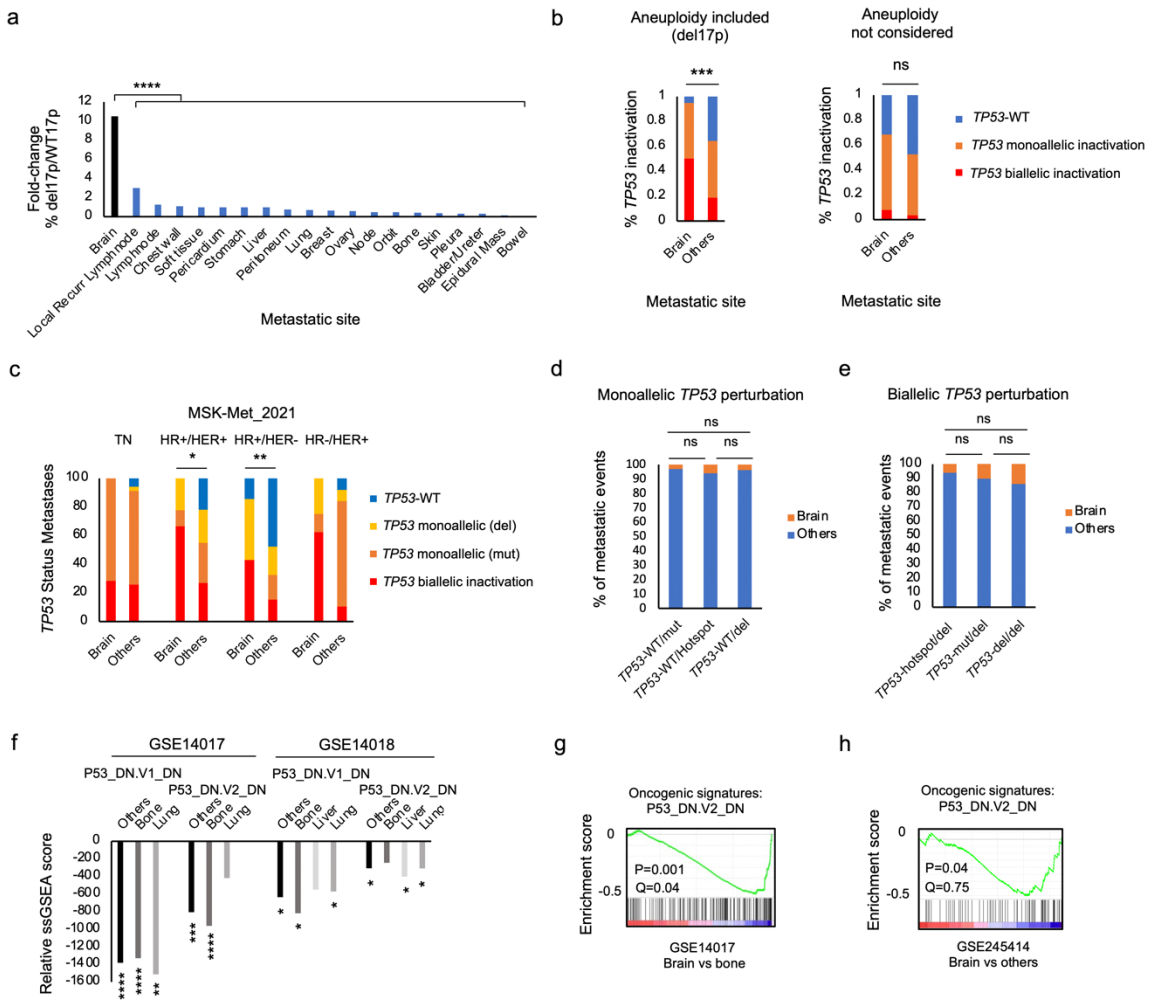

Supplementary Data Fig. 1: Clinical data analysis of *TP53* perturbation in BCBM (related to Fig. 1).

a, Prevalence of del17p in metastases from different metastatic sites, shown as fold-change over WT17p tumors using data from Razavi et al.[59]. Two-sided Fisher's exact test, brain compared to other metastatic sites, ****,$p=1*10^{-5}$. Tumor number: brain n=23, local recurrence n=4, lymph node n=83, chest wall n=56, soft tissue n=14, pericardium n=2, stomach n=2, lung n=24, breast n=10, ovary n=27, orbit n=3, bone n=98,skin n=15, pleura n=20, bladder/ureter n=4, epidural mass n=7, bowel n=7.

b, Prevalence of *TP53* perturbation in BCBM *vs*. other metastatic sites when considering aneuploidy calls (i.e., del17p) and without it (MSK-Met_2021). The enrichment of *TP53* alterations in BM over other sites is highly significant when chr17p copy-number status is considered. When chr17p status was not considered, the same trend was observed, but the result did not reach statistical significance. Two-sided Fisher's-exact test, *TP53*-WT *vs. TP53* inactivation: Aneuploidy-included ***,$p=1*10^{-4}$; aneuploidy-not-included p=0.07.

c, Comparison of the prevalence of *TP53* alterations in BM and other metastatic sites originating from breast tumors of different subtypes: Triple-Negative (TN), HR+/HER+, HR+/HER-, HR-/ HER+. One-sided Fisher's exact test, *TP53* inactivation *vs. TP53*-WT: Brain *vs.* others, TN p=0.5, HR+/HER+ p=0.18, HR+/HER-p=0.05, HR-/HER+ p=0.5; biallelic *TP53* inactivation *vs. TP53*-WT: Brain *vs.* others, TN p=0.5, HR+/HER+ *,p=0.04, HR+/HER-**,p=0.002, HR-/HER+ p=0.1. Tumor number TN: brain n=7, others n=136; HR+/HER+: brain n=9, others n=100; HR+/HER-: brain n=14, others n=569; HR-/HER+: brain n=8, others n=38.

d,e, The association between *TP53* perturbation and BM is not due to specific hotspot mutations. No difference in BM prevalence between different modes of (**d**) monoallelic and (**e**) biallelic *TP53* perturbation. *TP53* mutants with 3 common mutations (R175H, R273H, R248), *TP53* mutants with other point mutations, and del17p (with no other known *TP53* mutations) tumors were analyzed (\MSK_Met_2021). Two-sided Fisher's exact test.

TP53 monoallelic inactivation: *TP53*-WT/mut *vs.* WT/Hotspot p=0.23, *TP53*-WT/mut *vs. TP53*-WT/del p= 0.06, *TP53*-WT/ Hotspot *vs*. *TP53*-WT/del p=1. Tumor number: *TP53*-WT/mut n=218, *TP53*-WT/hotspot n=33, *TP53*-WT/del n=152.

biallelic *TP53* inactivation: *TP53*-mut/del *vs. TP53*-hotspot/del p=0.37, *TP53*-mut/del *vs. TP53*-del/del p=0.64, *TP53*-hotspot/del *vs.* del/del p=1. Tumor number *TP53*-mut/del n=150, *TP53*-hotspot/del n=12, *TP53*-del/del n=14.

f, Gene expression comparison between BMs and other metastatic sites by ssGSEA. p53 pathway activity scores are lower in BMs in comparison to other metastatic sites (GSE14017 and GSE14018), supplementing **Fig. 1f,g**. GSE14017: GSEA signature 'P53_DN.V1_DN', brain *vs.* others ****,$p=8*10^{-5}$, brain *vs.* bone, ***,$p=7*10^{-4}$, brain *vs.* lung **p=0.002. 'P53_DN.V2_DN' brain *vs.* others ***,$p=4*10^{-4}$, brain *vs.* bone ****,$p=9.8*10^{-5}$, brain *vs.* lung p=0.22. GSE14018: GSEA signature 'P53_DN.V1_DN', brain vs. others, *,p=0.02, brain *vs.* bone *,p=0.01, brain *vs.* liver p=0.18, brain *vs.* lung *,p=0.01. 'P53_DN.V2_DN' brain *vs.* others *,p=0.01, brain *vs.* bone p=0.05, brain *vs.* liver *,p=0.04, brain *vs.* lung *,p=0.04. Tumors GSE14017: Brain n=15, bone n=10, lung n=4. Tumors GSE14018: Brain n=7, bone n=9, liver n=5, lung n=16.

g, GSEA plot showing lower p53 pathway expression in BMs *vs.* bone metastases. Oncogenic signature 'P53_DN.V2_DN' **,p=0.001, FDR-corrected q=0.04. Brain n=15, bone n=10. See **Supplementary Table 2.**

h, GSEA plot showing lower p53 pathway expression in BMs *vs.* other metastases in a third, independent dataset (GSE245414). GSEA brain *vs.* others, oncogenic signature 'P53_DN.V2_DN' *,p=0.04. ssGSEA *,p=0.01. See **Supplementary Table 2**. Tumor number: brain n=6, others n= 26 (lymph nodes n=5, liver n=1, lung n=3, pleura n=3, soft tissue n=8, spine n=6).

Supplementary Fig.2

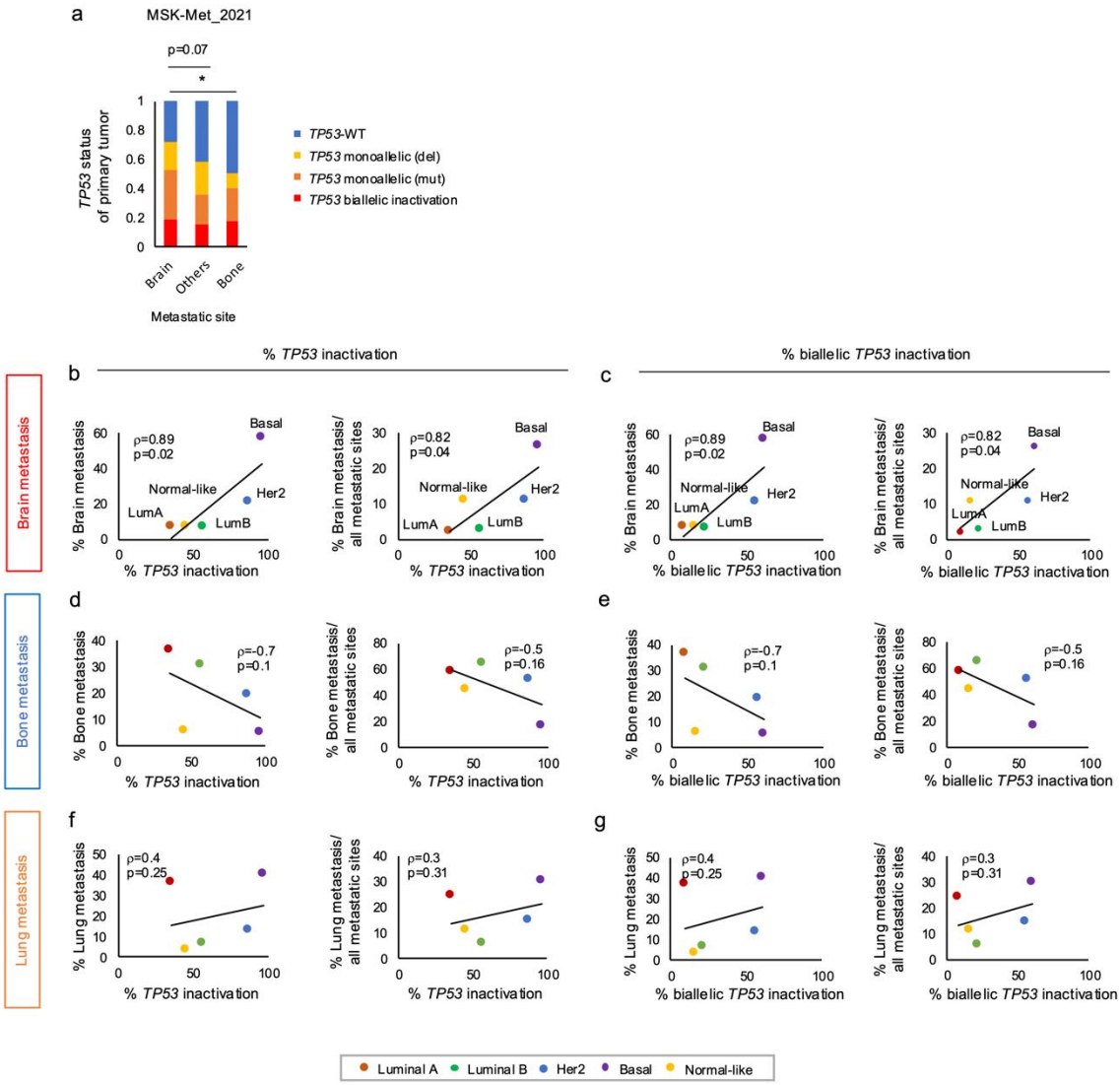

Supplementary Data Fig. 2: Prevalence of *p53* inactivation is associated with metastasis to the brain, but not to bone or lung, across BC subtypes (related to Fig. 1).

a, Prevalence of *TP53* alterations in primary breast tumors that metastasize to the brain compared to other metastatic sites. Data source: MSK-Met 2021. One-sided Fisher's exact test, *TP53*-inactivation *vs.* *TP53*-WT: brain *vs.* others p=0.07, brain *vs.* bone *,p=0.02. Brain n=32, others n=958, bone n=235. (Tumors that metastasized to >4 sites were excluded from the analysis.)
b,c, Significant positive correlation between *TP53* inactivation and BM prevalence across BC subtypes. Data source for *TP53* inactivation prevalence: METABRIC; Data source for BM prevalence: Smid et al., 2008[60]. **b,** Left: correlation between *TP53* inactivation prevalence and BM prevalence; ρ=0.89, one-sided p=0.02. Right: correlation between *TP53* inactivation and the relative fraction of BM out of all metastases; ρ=0.82, one-sided p=0.04. **c,** Left: correlation between biallelic *TP53* inactivation prevalence and BM prevalence; ρ=0.89, one-sided p=0.02. Right: correlation between biallelic *TP53* inactivation prevalence and the relative fraction of BM out of all metastases; ρ=0.82, one-sided p =0.04.

d-g, No significant correlation between *TP53* inactivation and the metastasis to other metastatic sites, as shown for two common metastatic sites of BC, bone and lung. **d,e,** Trending negative correlation between *TP53* inactivation and bone metastasis prevalence. **d,** Left: correlation between *TP53* inactivation prevalence and bone metastasis prevalence; ρ=-0.7, p=0.1. Right: correlation between *TP53* inactivation and the relative fraction of bone metastasis out of all metastases; ρ=-0.5, p =0.16. **e,** Left: correlation between biallelic *TP53* inactivation prevalence and bone metastasis prevalence; ρ=-0.7, p =0.1. Right: correlation between biallelic *TP53* inactivation prevalence and the relative fraction of bone metastasis out of all metastases; ρ = -0.5, p=0.16. **f,g,** No significant correlation between *TP53* inactivation and lung metastasis prevalence. **f**, Left: correlation between *TP53* inactivation prevalence and lung metastasis prevalence; ρ=0.4, p=0.25. Right: correlation between *TP53* inactivation and the relative fraction of lung metastasis out of all metastases; ρ=0.31, p=0.3. **g,** Left: correlation between biallelic *TP53* inactivation prevalence and lung metastasis prevalence; ρ=0.4, p =0.25. Right: correlation between biallelic *TP53* inactivation prevalence and the relative fraction of lung metastasis out of all metastases; ρ=0.31, p =0.3. (Note that the Spearman correlation coefficients and p-values are identical in panels 'b' *vs.* 'c', 'd' *vs.* 'e', and 'f' *vs.* 'g', due to the same ranking of observations.) See **Source Data**.

Supplementary Fig.3

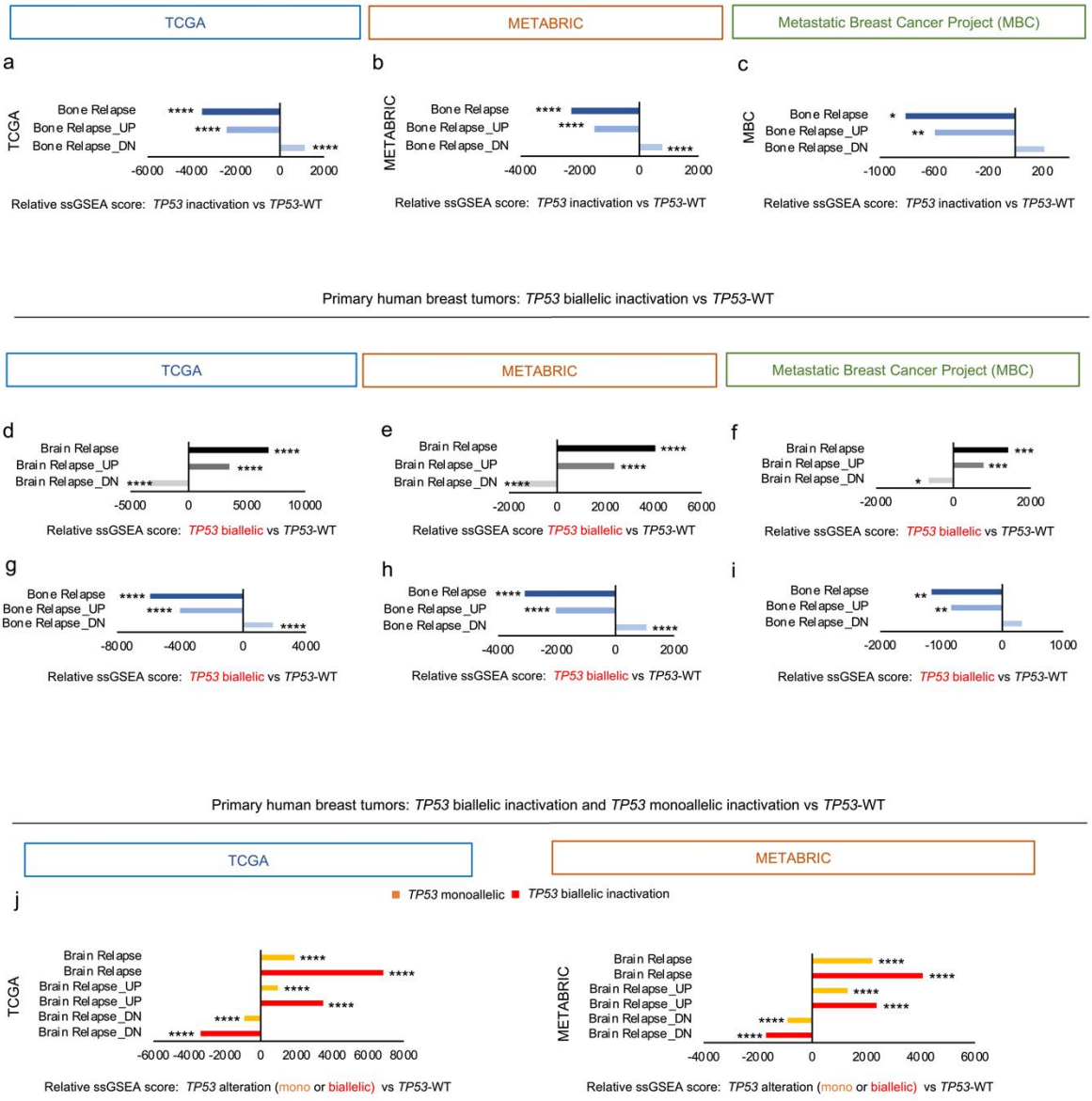

Primary human breast tumors: Breast Cancer Subtypes

k

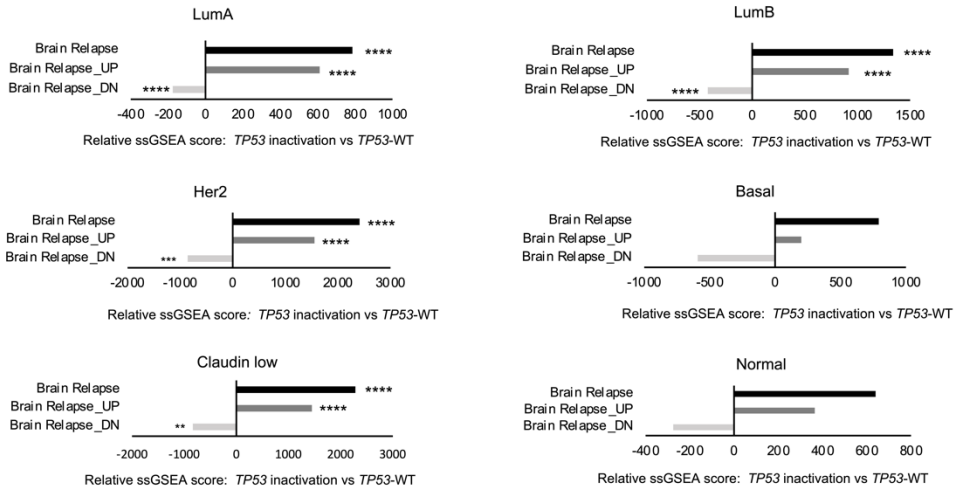

Human BC cell lines (CCLE)

l

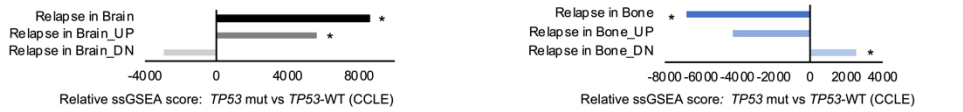

m

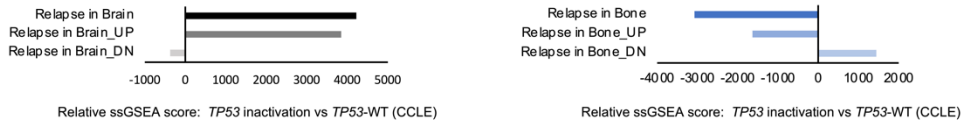

n

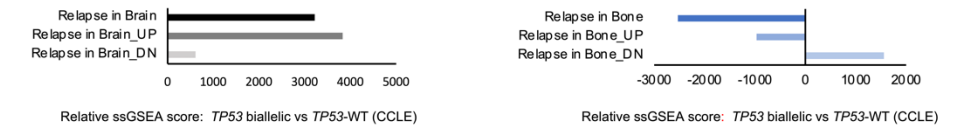

Supplementary Data Fig. 3: Gene set enrichment analysis of gene expression data from primary human breast tumors and breast cancer cell lines (related to Fig. 1).

a-c, ssGSEA comparing gene expression signatures associated with bone metastasis between human primary BCs with *TP53* inactivation *vs. TP53*-WT tumors in TCGA (**a**), METABRIC (**b**) and MBC (**c**). Gene expression signatures associated with bone metastasis are lower in primary tumors that harbor *TP53* alterations. Note that this trend is opposite to that observed with BM-associated gene signatures.

TCGA: 'Smid_breast_cancer_relapse_in_bone' ****,p=$1.8*10^{-42}$, 'Smid_breast_cancer_relapse_in_bone_up' ****,p=$9.6*10^{-53}$, 'Smid_breast_cancer_relapse_in_bone_dn ****,p=$5.9*10^{-54}$. Two-sided t-test.

METABRIC: 'Smid_breast_cancer_relapse_in_bone' ****,p=$1.2*10^{-19}$, 'Smid_breast_cancer_relapse_in_bone_up' ****,p=$4.4*10^{-25}$, 'Smid_breast_cancer_relapse_in_bone_dn' ****,p=$2.6*10^{-24}$. Two-sided t-test.

MBC: 'Smid_breast_cancer_relapse_in_bone' *,p=0.03, 'Smid_breast_cancer_relapse_in_bone_up' **,p=0.008, 'Smid_breast_cancer_relapse_in_bone_dn' p=0.23. Two-sided t-test.

d-i, ssGSEA comparing gene expression signatures associated with brain and bone metastases in BCs with biallelic *TP53* inactivation *vs. TP53*-WT tumors in TCGA (**d,g**), METABRIC (**e,h**) and MBC (**f,i**). Note the opposing trends between brain and bone signatures. See **Supplementary Table 4**.

TCGA: 'Smid_breast_cancer_relapse_in_brain' ****,p=$7.6*10^{-50}$, 'Smid_breast_cancer_relapse_in_brain_up' ****,p=$2.1*10^{-46}$, 'Smid_breast_cancer_relapse_in_brain_dn' ****,p=$3.6*10^{-48}$. 'Smid_breast_cancer_relapse_in_bone' ****,p=$9.3*10^{-52}$, 'Smid_breast_cancer_relapse_in_bone_up' ****,p=$2.6*10^{-53}$ 'Smid_breast_cancer_relapse_in_bone_dn' ****,p=$6*10^{-42}$. Two-sided t-test.

METABRIC: 'Smid_breast_cancer_relapse_in_brain' ****,p=$1.7*10^{-76}$, 'Smid_breast_cancer_relapse_in_brain_up' ****,p=$7.8*10^{-79}$,, 'Smid_breast_cancer_relapse_in_brain_dn' ****,p=$3.2*10^{-60}$, 'Smid_breast_cancer_relapse_in_bone' ****p=$6.5*10^{-68}$, 'Smid_breast_cancer_relapse_in_bone_up' ****p=$1*10^{-65}$, 'Smid_breast_cancer_relapse_in_bone_dn' ****,p=$7*10^{-53}$. Two-sided t-test.

MBC: 'Smid_breast_cancer_relapse_in_brain' ***,p=$7*10^{-4}$, 'Smid_breast_cancer_relapse_in_brain_up' ***,p=$2*10^{-4}$, 'Smid_breast_cancer_relapse_in_brain_dn' *,p=0.01, 'Smid_breast_cancer_relapse_in_bone' **,p=0.004, 'Smid_breast_cancer_relapse_in_bone_up' **,p=0.002, ''Smid_breast_cancer_relapse_in_bone_dn' p=0.11. Two-sided t-test.

j, ssGSEA comparing gene expression signatures associated with BM between monoallelic or biallelic *TP53* inactivation *vs. TP53*-WT tumors in TCGA and METABRIC. Gene expression signatures associated with BM already increased in primary tumors that harbor monoallelic *TP53* alterations.

TCGA: Two-sided t-test, monoallelic *TP53* inactivation *vs. TP53*-WT, 'Smid_breast_cancer_relapse_in_brain' ****,p=$1.6*10^{-8,}$,

'Smid_breast_cancer_relapse_in_brain_up' ****,p=$9.3*10^{-8}$, 'Smid_breast_cancer_relapse_in_brain_dn' ****,p=$2.6*10^{-8}$; biallelic *TP53* inactivation *vs.* *TP53*-WT, 'Smid_breast_cancer_relapse_in_brain' ****,p=$7.6*10^{-50}$, 'Smid_breast_cancer_relapse_in_brain_up' ****,p=$2.1*10^{-46}$, 'Smid_breast_cancer_relapse_in_brain_dn' ****,p=$3.6*10^{-48}$. METABRIC: Two-sided t-test, monoallelic *TP53* inactivation *vs.* *TP53*-WT, 'Smid_breast_cancer_relapse_in_brain' ****,p=$5*10^{-29}$, 'BRAIN_UP' ****,p=$1.3*10^{-29}$, 'Smid_breast_cancer_relapse_in_brain_dn' ****,p=$4.1*10^{-23}$; biallelic *TP53* inactivation *vs.* *TP53*-WT, 'Smid_breast_cancer_relapse_in_brain' ****,p=$1.7*10^{-76}$, 'Smid_breast_cancer_relapse_in_brain_up' ****,p=$7.8*10^{-79}$, ''Smid_breast_cancer_relapse_in_brain_dn' ****,p=$3.2*10^{-60}$. Note that the comparisons of biallelic *TP53* inactivation *vs.* *TP53*-WT tumors are the same as in **d,e**.

k, ssGSEA comparing gene expression signatures associated with BM between BCs with *TP53* perturbation to *TP53*-WT tumors in METABRIC. Tumors were stratified by BC molecular subtypes to rule out subtype as a confounder in the association analysis. BM signatures are elevated in primary BC with *TP53* perturbation across all molecular subtypes. METABRIC, two-sided t-test, *TP53* inactivation *vs.* *TP53*-WT:

LumA: 'Smid_breast_cancer_relapse_in_brain' ****,p=$9.7*10^{-11}$, 'Smid_breast_cancer_relapse_in_brain_up' ****,p=$3.7*10^{-10}$, 'Smid_breast_cancer_relapse_in_brain_dn' ****,p=$6.4*10^{-16}$;

LumB: 'Smid_breast_cancer_relapse_in_brain' ****,p=$2.3*10^{-13}$, 'Smid_breast_cancer_relapse_in_brain_up' ****,p=$2.5*10^{-12}$, ''Smid_breast_cancer_relapse_in_brain_dn' ****,p=$7.5*10^{-10}$;

Her2: 'Smid_breast_cancer_relapse_in_brain' ****,p=$5.9*10^{-6}$, 'Smid_breast_cancer_relapse_in_brain_up' ****, p=$5.8*10^{-6}$, 'Smid_breast_cancer_relapse_in_brain_dn' ***,p=$4*10^{-4}$;

Basal: 'Smid_breast_cancer_relapse_in_brain' p=0.4, 'Smid_breast_cancer_relapse_in_brain_up' p=0.6, 'Smid_breast_cancer_relapse_in_brain_dn' p=0.3;

Claudin-low: 'Smid_breast_cancer_relapse_in_brain' ****,p=$9.6*10^{-7}$, 'Smid_breast_cancer_relapse_in_brain_up' ****,p=$4*10^{-9}$, 'Smid_breast_cancer_relapse_in_brain_dn' **,p=0.001;

Normal: 'Smid_breast_cancer_relapse_in_brain' p=0.1, 'Smid_breast_cancer_relapse_in_brain_up' p=0.14, 'Smid_breast_cancer_relapse_in_brain_dn' p=0.13.

Number of tumors: LumA: *TP53* inactivated n=177, *TP53*-WT n=323; LumB: *TP53* inactivated n=163, *TP53*-WT n=128; Her2: *TP53* inactivated n=120, *TP53*-WT n=18; Basal: *TP53* inactivated n=142, *TP53*-WT n=6; Claudin-low: *TP53* inactivated n=94, *TP53*-WT n=62; Normal: *TP53* inactivated n=45, *TP53*-WT n=54.

l-n, ssGSEA comparing gene expression signatures associated with brain and bone metastases between human BC cell lines with or without *TP53* perturbation (n=43). **l,** Increased expression of signatures associated with BM (left) and decreased expression of signatures associated with bone metastasis (right). One-sided t-test, *TP53*-mut versus *TP53*-WT, brain: 'Smid_breast_cancer_relapse_in_brain' *,p=0.02, 'Smid_breast_cancer_relapse_in_brain_up' *,p=0.01, 'Smid_breast_cancer_relapse_in_brain_dn' p=0.11; bone:

‘Smid_breast_cancer_relapse_in_bone’ *,p=0.04, ‘Smid_breast_cancer_relapse_in_bone_up’ p= 0.07, ‘Smid_breast_cancer_relapse_in_bone_dn’ *,p=0.02. The same trend was observed when comparing any *TP53* inactivation to *TP53*-WT (**m**) and *TP53* biallelic inactivation to *TP53*-WT (**n**), although it did not reach significance. *TP53* inactivation *vs. TP53*-WT, brain: ‘Smid_breast_cancer_relapse_in_brain’ p=0.18, ‘Smid_breast_cancer_relapse_in_brain_up’ p=0.07, ‘‘Smid_breast_cancer_relapse_in_brain_dn’ p=0.43; bone: ‘Smid_breast_cancer_relapse_in_bone’ p=0.22, ‘Smid_breast_cancer_relapse_in_bone_up’ p=0.28, ‘Smid_breast_cancer_relapse_in_bone_dn’ p=0.16. *TP53* biallelic inactivation *vs. TP53*-WT, brain: ‘Smid_breast_cancer_relapse_in_brain’ p=0.25, ‘Smid_breast_cancer_relapse_in_brain_up’ p=0.09, ‘BRAIN_DN’ P=0.38; bone: ‘Smid_breast_cancer_relapse_in_bone’ p=0.25, ‘Smid_breast_cancer_relapse_in_bone_up’ p=0.36, ‘Smid_breast_cancer_relapse_in_bone_dn’ p=0.15. BC cell lines, *TP53*-WT: n=4, *TP53*-mut: n=20, *TP53* inactivated: n=43, *TP53*-null: n=16. See **Source Data**.

Supplementary Fig.4

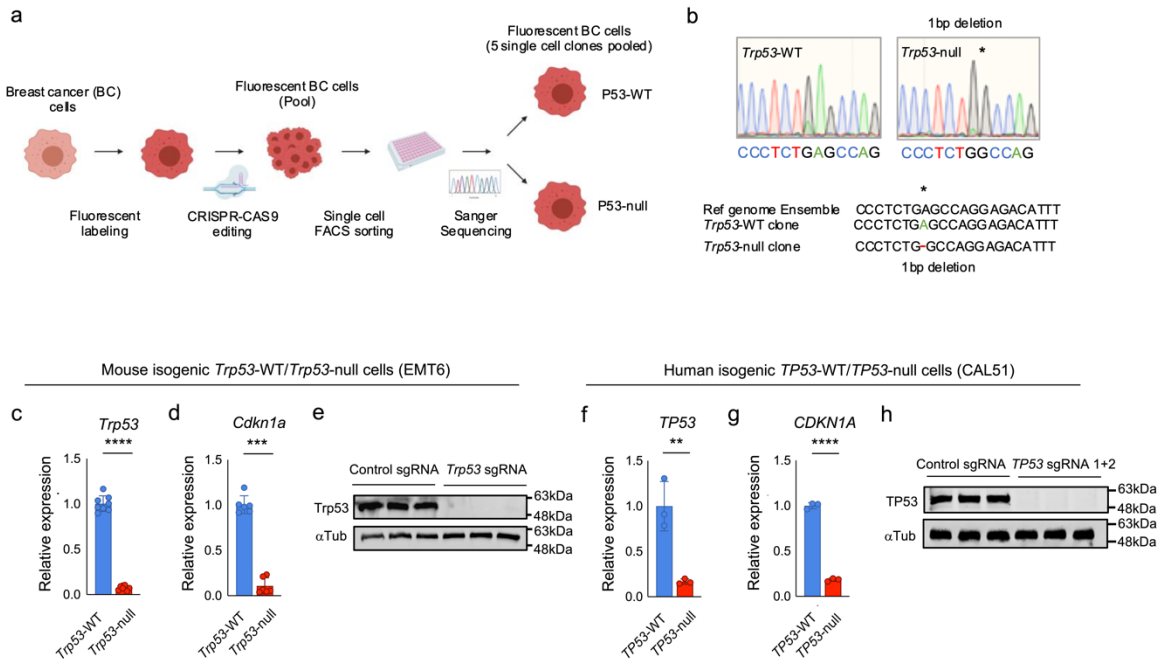

Supplementary Data Fig. 4: Generation of mouse and human isogenic *Trp53*/*TP53*-WT and *Trp53*/*TP53*-null BC cells (related to Fig. 2).

a, Schematic illustration of isogenic cell line generation of *Trp53*-WT and *Trp53*-null BC cells. Murine EMT6 cells were fluorescently labeled, subjected to CRISPR-Cas9 editing targeting *Trp53* and subsequently sorted and grown as single cell clones. *Trp53* status was assessed by Sanger sequencing. Human *TP53*-null CAL51 cells were generated in the same way, except without single-cell sorting, resulting in a heterogeneous population of *TP53*-null cells.

b, Sanger sequencing confirmed *Trp53*-WT and *Trp53*-null status of EMT6 single cell-derived clones. Shown is an example for one such clone. Five independent single cell-derived clones were mixed per genotype to obtain the *Trp53*-WT/*Trp53*-null isogenic models.

c-e, Validation of mouse EMT6 isogenic *Trp53*-WT/*Trp53*-null system. **c,** qPCR measurement of *Trp53* mRNA levels: *Trp53*-null cells show a strong (93%) reduction in *Trp53* mRNA levels. One-sided t-test, ****,$p=2.7*10^{-14}$. *Trp53*-WT: n=8, *Trp53*-null: n=8. Error Bars, mean +/- SD. **d,** qPCR measurement of the mRNA levels of the p53 target p21 (*Cdkn1A*), showing that it is drastically decreased (90% reduction) in EMT6 *Trp53*-null cells. One-sided t-test, ****,$p=7.1*10^{-6}$. *Trp53*-WT: n=6, *Trp53*-null: n=6. Error Bars, mean +/- SD. **e,** Western blot showing abundant p53 protein in *Trp53*-WT EMT6 cells, but no p53 protein in their isogenic *Trp53*-null EMT6 cells. *Trp53*-WT: n=3, *Trp53*-null: n=2.

f-h, Validation of human CAL51 isogenic *TP53*-WT/*TP53*-null system. **f,** qPCR measurement of *TP53* mRNA levels: *TP53*-null cells show a strong (83%) reduction in *TP53* mRNA levels. One-sided t-test, sgRNA-*TP53 vs.* sgRNA-control, **,p=0.003. *Trp53*-WT n=3, *Trp53*-null n=3. Error Bars, mean +/- SD. **g,** qPCR measurement of the mRNA levels of the p53 target p21 (*CDKN1A*), showing that it is decreased (81% reduction) in CAL51 *TP53*-null cells. One-sided t-test, ****,$p=2*10^{-6}$. *Trp53*-WT: n=3, *Trp53*-null: n=3. Error Bars, mean +/- SD. **h,** Western blot showing abundant p53 protein in *TP53*-WT CAL51 cells, but no p53 protein in their isogenic *TP53*-null CAL51 cells. See **Source Data**. **Supplementary data Fig. 4a** created with BioRender.com.

Supplementary Fig.5

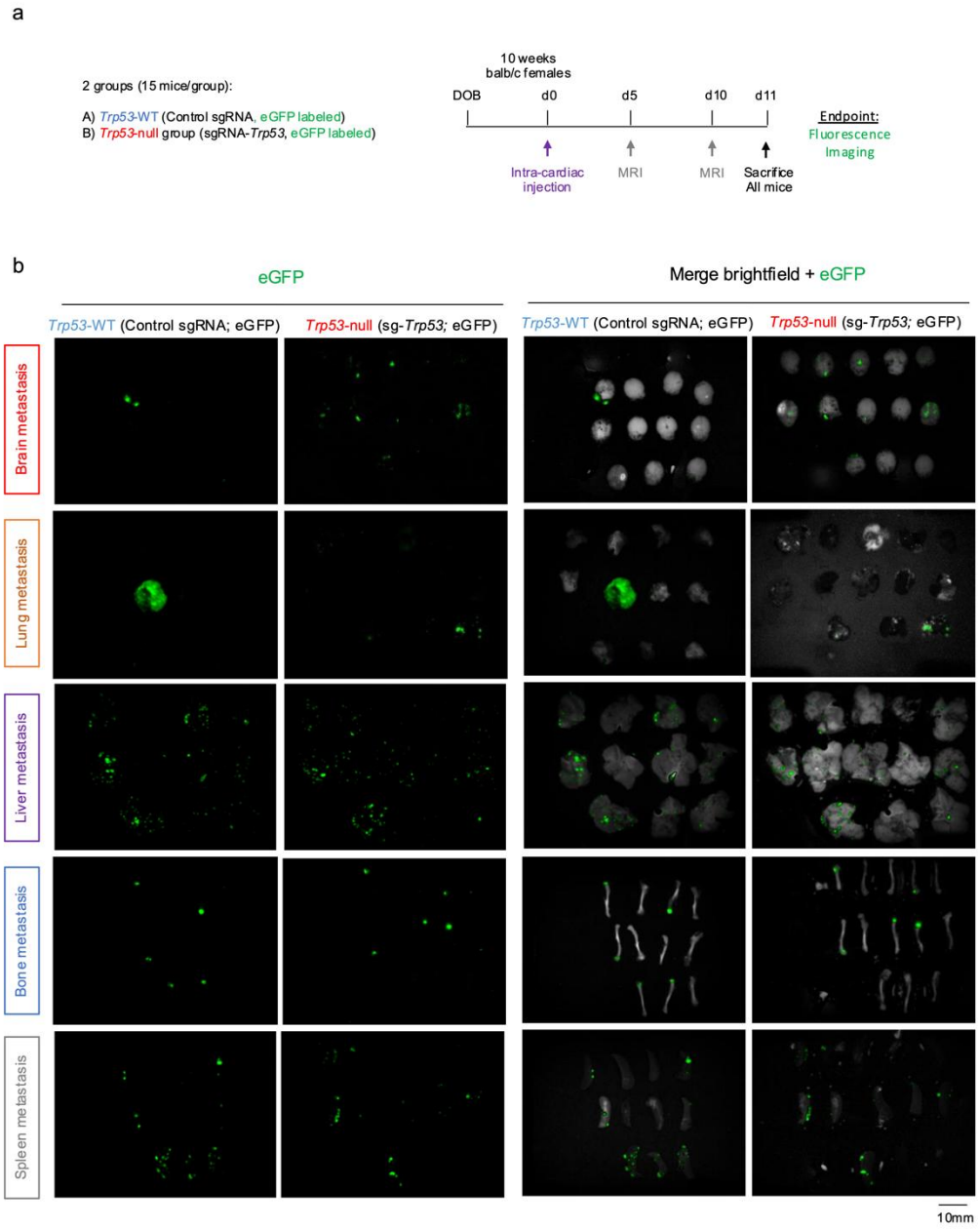

Supplementary Data Fig. 5: Brain organotropism of mouse *Trp53*-WT and *Trp53*-null EMT6 isogenic cells following intra-cardiac injection into separate immune-competent mice (related to Fig. 2).

a, Experimental timeline of intra-cardiac injections of *Trp53*-WT and *Trp53*-null isogenic EMT6 cells. Two groups of 15 mice each were injected with either *Trp53*-WT or *Trp53*-null cells, both fluorescently labeled with eGFP. The entire cohort was sacrificed when mice started to die at day 11. At the endpoint, five organs (brain, lung, liver, bone, spleen) were harvested and eGFP fluorescence and brightfield images were taken from each.

b, eGFP fluorescence images (left) or a merge of eGFP fluorescence and brightfield images (right) of five organs dissected from mice that had been injected with *Trp53*-WT or *Trp53*-null isogenic cells. Shown are brain, lung, liver, bone and spleen. *Trp53*-WT: n=11, *Trp53*-null: n=13.

c, Additional quantification of tumor burden following intra-cardiac injection of *Trp53*-WT or *Trp53*-null EMT6 cells, supplementing **Fig. 2h**. Brain tumor burden was calculated as the intensity of fluorescent signal relative to organ size. *Trp53*-null *vs.* *Trp53*-WT injected mice, two-sided t-test: brain *,p=0.03, lung p=0.48, liver p=0.63, bone p=0.75, spleen p=0.49. *Trp53*-WT: n=11, *Trp53*-null: n=13. Boxplots: bar = median; box = 25–75th percentile; whiskers = range. See **Source Data**.

Supplementary Fig.6

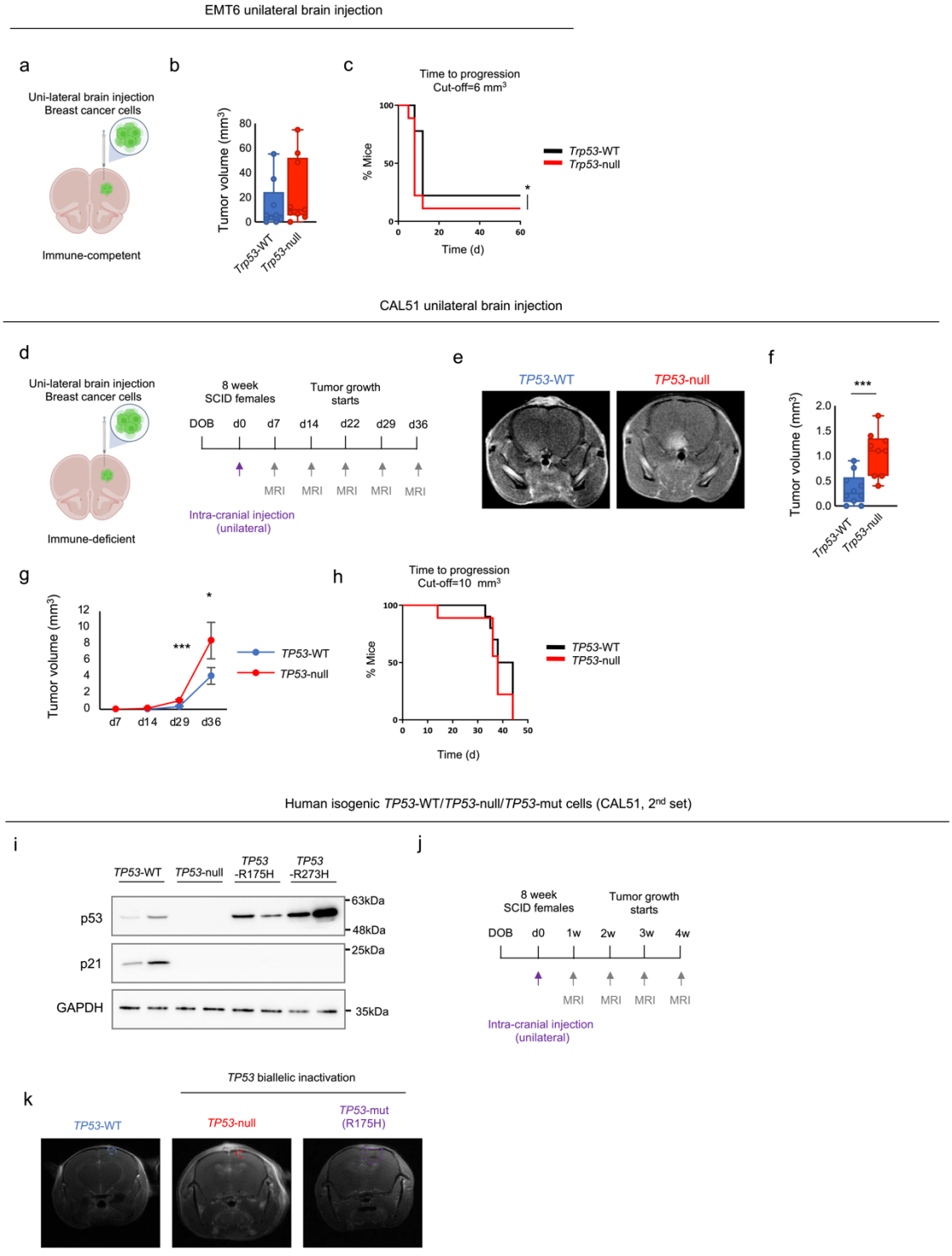

Supplementary Data Fig. 6: Intra-cranial injections of mouse and human *Trp53*-WT/*TP53*-WT and *Trp53*-null/*TP53*-null cells (related to Fig. 2).

a, Schematic illustration of unilateral intra-cranial injection of isogenic *Trp53*-WT and *Trp53*-null mouse BC cells into immune-competent mice. Mice were injected with either *Trp53*-WT or *Trp53*-null EMT6 cells directly into the brain (two mouse cohorts, n=10 per group).

b, MRI-based quantification of tumor volume 8 days after unilateral intra-cranial injection. Brain tumors from injected EMT6 *Trp53*-null cells were larger than those from *Trp53*-WT cells. One-sided Mann-Whitney test, ns ,p=0.11. *Trp53*-WT: n=9, *Trp53*-null: n=9.

c, Time to progression analysis. *Trp53*-null tumors reached a size threshold ($6mm^3$) faster than their isogenic controls. Two-sided Gehan-Breslow-Wilcoxon test, *,p=0.035. *Trp53*-WT: n=9, *Trp53*-null: n=9.

d, Schematic illustration of unilateral intra-cranial injection of isogenic *TP53*-WT and *TP*53-null human BC cells into immune-deficient (SCID) mice. Mice were injected with either *TP53*-WT or *TP53*-null CAL51 cells directly into the brain (two mouse cohorts, n=10 per group). The experimental timeline is shown, brains were imaged by MRI throughout a five-week period.

e, Representative MRI images of mouse brains 36 days after unilateral intra-cranial injection of the isogenic cells.

f,g, MRI-based quantification of tumor volume following intra-cranial injection. **f**, Comparison of tumor volume 29 days after injection. **g**, Tumor growth over time. One-sided t-test, d29 ****,$p=4*10^{-5}$, d36 *,p=0.049. *TP53*-WT: n=10, *TP53*-null: n=9.

h, Time to progression analysis. *TP53*-null tumors reached a size threshold ($10mm^3$) faster (albeit not significantly) than their isogenic controls. Two-sided Gehan-Breslow-Wilcoxon test, p=0.37, *TP53*-WT: n=10, *TP53*-null: n=9.

i, Validation of an independently generated human CAL51 isogenic system, consisting of *TP53*-WT, *TP53*-null, *TP53*-mut (R175H/R175H) and *TP53*-mut (R273H/R273H) cells. Western blot analysis shows the absence of the p53 target p21 in cells with p53 alterations. n=4.

j, Experimental timeline for unilateral intra-cranial injection of *TP53*-WT, *TP*53-null and *TP53*-mut (R175H/R175H) cells into immune-deficient (SCID) mice. Note that this is a second, independently generated isogenic CAL51 system. Brains were imaged by MRI throughout a four-week period.

k, Representative MRI images of mouse brains 4 weeks after unilateral intra-cranial injection of the isogenic cells**.** See quantification in **Fig. 2p**. Boxplots: bar = median; box = 25–75th percentile; whiskers = range. See **Source Data**. **Supplementary data Fig. 6a,d** created with BioRender.com.

Supplementary Fig.7

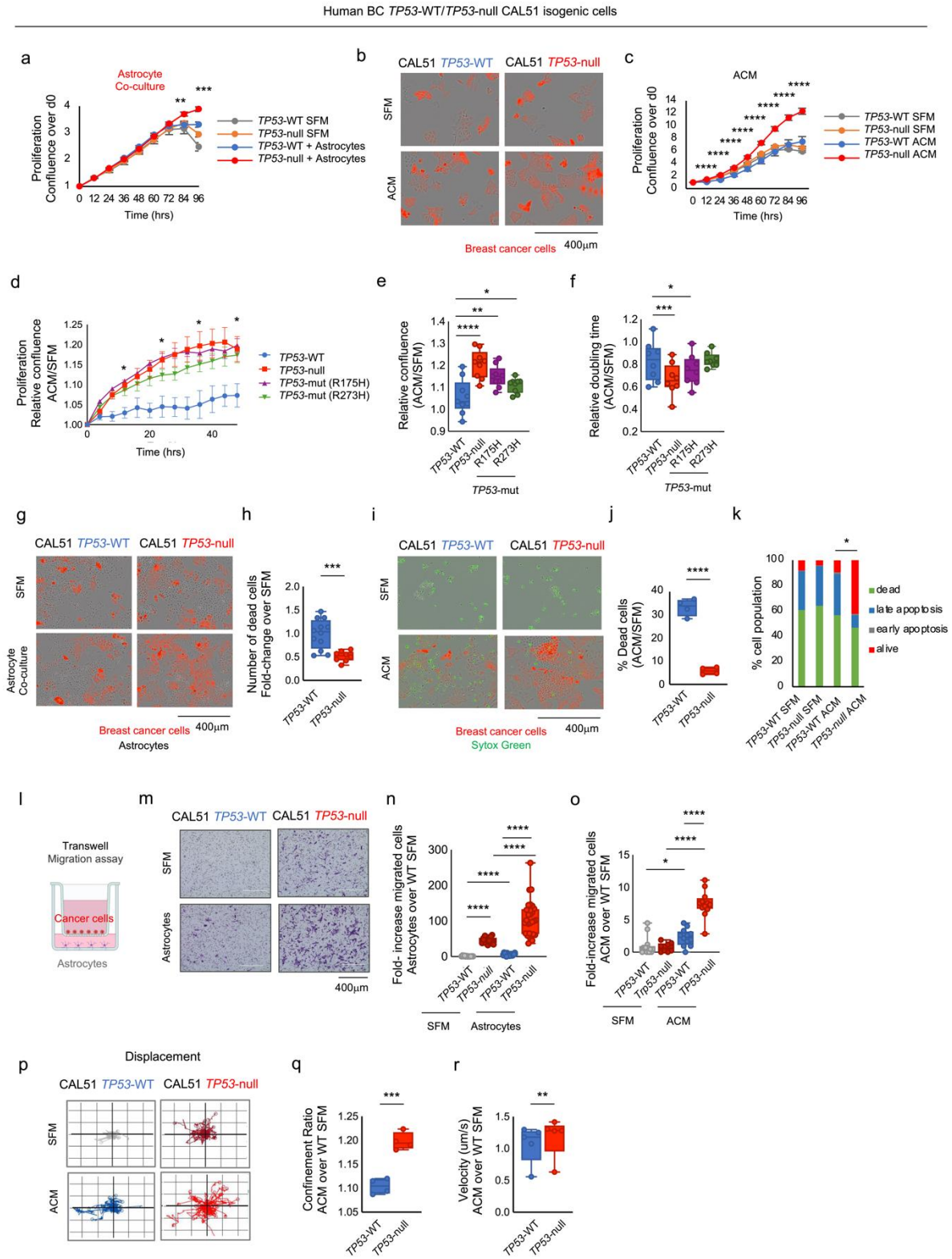

Supplementary Data Fig. 7: Human astrocytes infiltrate p53-null BMs and promote the survival, proliferation and migration of p53-null BC cells in the brain (related to Fig. 3).

a, Live imaging-based proliferation of CAL51 cells co-cultured with activated astrocytes; stronger effect in *TP53*-null *vs. TP53*-WT. One-sided t-test, 84hrs: **,p=0.002; 96hrs: ***,p=$1*10^{-4}$. *TP53*-WT: n=8, *TP53*-null: n=8. Error Bars, mean +/- SEM.

b, Images of *TP53*-WT and *TP53*-null CAL51 cells grown for 48hrs in SFM or ACM. *TP53*-null cells cultured in ACM had a growth advantage over their isogenic *TP53*-WT and SFM controls.

c, Proliferation curves of CAL51 cells cultured in ACM or SFM. One-sided t-test, 12hrs ****,p=$1*10^{-7}$; 24hrs ****,p=$5*10^{-7}$; 36hrs ****,p=$3*10^{-5}$; 48hrs ****,p=$5*10^{-6}$; 60hrs ****,p=$4*10^{-6}$; 72hrs ****,p=$5*10^{-6}$; 84hrs ****,p=$5*10^{-6}$; 96hrs ****,p=$3*10^{-5}$. *TP53*-WT: n=20, *TP53*-null: n=20. Error Bars, mean +/- SEM.

d, Live imaging-based proliferation of CAL51 cells. ACM promotes proliferation to a greater extent in *TP53*-null/mut *vs. TP53*-WT cells. Note that this is a second, independently generated isogenic CAL51 system. One-sided t-test, *TP53*-WT *vs. TP53*-null: 12hrs *,p=0.01, 24hrs *,p=0.01, 36hrs *,p=0.02, 48hrs *,p=0.03; *TP53*-WT *vs. TP53*-mut (R175H/R175H): 12hrs **,p=0.002 24hrs, **,p=0.006, 36hrs *,p=0.02, 48hrs *,p=0.01; *TP53*-WT *vs. TP53*-mut (R273H/R273H): 12hrs *,p=0.02 24hrs *,p=0.03, 36hrs *,p=0.03, 48hrs *,p=0.02. Error bars, mean +/- SEM.

e, Proliferation at 24hrs (ACM/SFM) was higher in *TP53*-null/mut than in *TP53*-WT cells. Paired one-sided t-test, *TP53*-WT *vs. TP53*-null ****,p=$1.4*10^{-5}$, *TP53*-WT *vs. TP53*-mut (R175H/R175H) **,p=0.001, *TP53*-WT *vs. TP53*-mut (R273H/R273H) *,p=0.03. n=9.

f, Relative doubling time (ACM): faster doubling time in *TP53*-null and *TP53*-mut (R175H) *vs. TP53*-WT (Paired one-sided t-test, *TP53*-WT *vs. TP*53-null cells ***,p=$5*10^{-4}$; *TP53*-WT *vs. TP53*-mut (R175H) cells *,p=0.01. n=8.

g, Images of *TP53*-WT and *TP53*-null CAL51 cells co-cultured with activated human astrocytes.

h, Cell death quantification by morphology. *TP53*-null CAL51 cells showed reduced cell death, evaluated by their morphology, when co-cultured with activated human astrocytes (72hrs). One-sided t-test, ***,p=$4*10^{-4}$. Number of fields: *TP53*-WT n=10, *TP53*-null n=7.

i, Images of *TP53*-WT and *TP53*-null CAL51 cells cultured in SFM or ACM for 5 days and stained with Sytox green.

j, Cell death quantification by Sytox green. ACM rescued cell death to a greater extent in *T53*-null *vs*. *TP53*-WT cells. Dying cells (green) and living cells (red) shown as percentage of cell population. Two-sided t-test, ****,p=$1*10^{-5}$. *TP53*-WT: n=4, *TP53*-null: n=4.

k, Apoptosis quantification by flow cytometry: apoptosis was measured in *TP53*-WT and *TP53*-null CAL51 cultured in ACM for 3 days (AnnexinV/Sytox green). The fraction of living cells was higher for *TP53*-null cells. Two-sided Chi^2-test, *,p=0.03. *TP53*-WT: n=3, *TP53*-null: n=3. See **Supplementary Fig. 16b**.

l-o, Transwell migration assays. **l,** Schematic illustration. **m,** Representative images. **n,** *TP53*-null CAL51 cells migrate more already in SFM, and astrocytes further increase their migration. One-sided t-test, SFM *TP53*-WT *vs. TP53*-null ****,p=$2.3*10^{-16}$; Astrocytes *TP53*-null *vs. TP53*-WT grown with astrocytes ****,p=$2.6*10^{-10}$; *TP53*-WT: Astrocytes *vs.* SFM

****p=5.9*10^{-5}; *TP53*-null: Astrocytes *vs.* SFM ****,p=1*10^{-5}. Relative Astrocytes/SFM: *TP53*-WT *vs. TP53*-null ****,p=2*10^{-5}. Fields counted: *TP53*-WT n=26, *TP53*-null n=28. **o,** ACM promoted CAL51 cell migration to a much greater extent in *TP53*-null *vs. TP53*-WT cells. One-sided t-test, ACM: *TP53*-null *vs. TP53*-WT ****,p=1.3*10^{-7}; *TP53*-WT: SFM *vs.* ACM *,p=0.01; *TP53*-null: SFM *vs.* ACM ****,p=3.2*10^{-8}. Fields counted: *TP53*-WT n=12, *TP53*-null n=12.

p-**r**, Live imaging of ACM-treated CAL51 cells. **p,** Representative cell tracking plots. **q,** ACM increased cell motility in both genotypes, but to a greater extent in *TP53*-null cells. Shown as confinement ratio ACM/SFM (one-sided t-test, ***,p=5*10^{-4}, n=4). **r,** ACM increased cell velocity in both genotypes, but to a greater extent in *TP53*-null cells. ACM/SFM (one-sided t-test **,p=0.004. *TP53*-WT: n=5, *TP53*-null: n=5). Shown as the velocity ratio ACM/SFM. n=38. Boxplots: bar = median; box = 25–75th percentile; whiskers = range. See **Source Data**.

Supplementary Fig.8

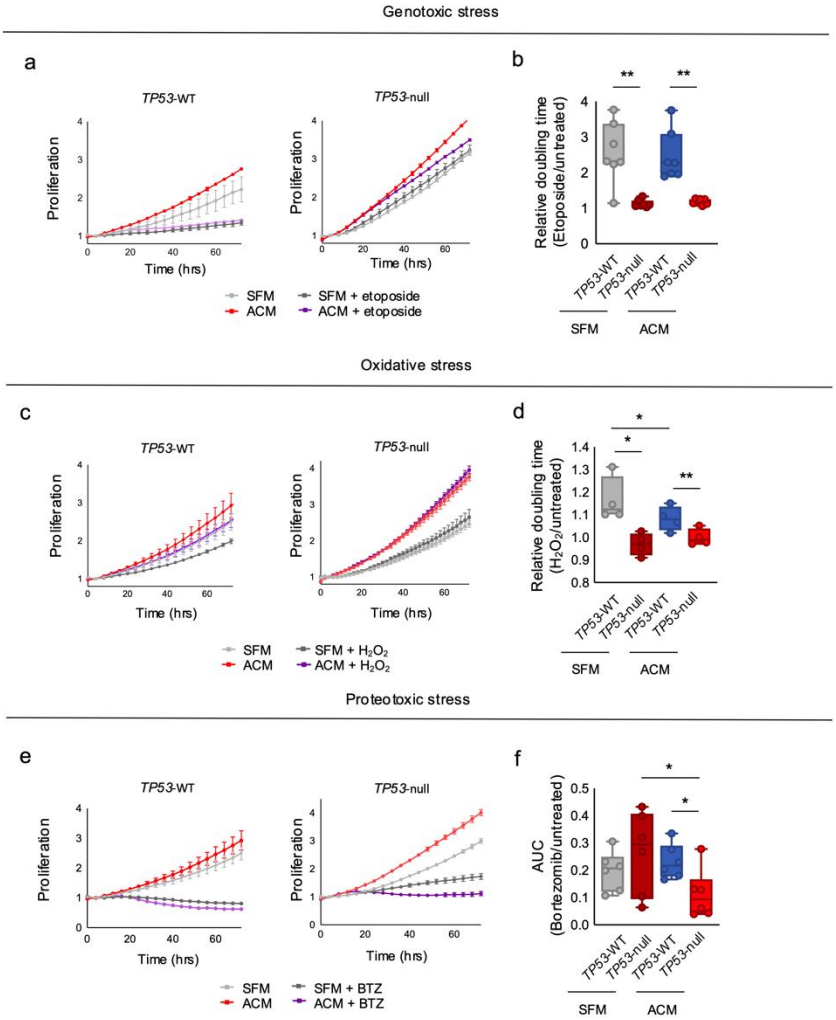

Supplementary Data Fig. 8: Human ACM does not always protect human BC cells from stress, and such protection is not always p53-dependent (related to Fig. 3).

a,b, The effect of ACM and *TP53* status on cellular response to genotoxic stress. **a,** Proliferation curves of CAL51 cells exposed to etoposide (150nM) in SFM or ACM: *TP53*-null cells are more resistant to genotoxic stress, as expected. ACM does not protect from genotoxic stress regardless of the *TP53* status. **b,** Doubling time quantification. Paired one-sided t-test, *TP53*-null *vs.* *TP53*-WT etoposide in SFM **,p=0.002; *TP53*-null *vs.* *TP53*-WT etoposide in ACM **,p=0.002; *TP53*-WT etoposide in ACM *vs.* *TP53*-WT etoposide in SFM p=0.1; *TP53*-null etoposide in ACM *vs.* *TP53*-null etoposide in SFM p=0.41. n=7.

c,d, The effect of ACM and *TP53* status on cellular response to oxidative stress. **c,** Proliferation curves of CAL51 cells exposed to H_2O_2 (4μM) in SFM or ACM: *TP53*-null cells tolerate oxidative stress better than *TP53*-WT controls. ACM protects cells from oxidative stress, and its protective effect is stronger in *TP53*-WT cells. **d,** Doubling time quantification. Paired one-sided t-test, *TP53*-null *vs.* *TP53*-WT H_2O_2 in SFM p=0.03; *TP53*-null *vs.* *TP53*-WT H_2O_2 in ACM p=0.004; *TP53*-WT H_2O_2 in ACM *vs.* *TP53*-WT H_2O_2 in SFM p=0.03; *TP53*-null H_2O_2 in ACM *vs.* *TP53*-null H_2O_2 in SFM p=0.25. n=4.

e,f, The effect of ACM and *TP53* status on cellular response to proteotoxic stress. **e,** Proliferation curves of CAL51 cells exposed to bortezomib (2nM) in SFM or ACM: ACM is detrimental for cell proliferation under proteotoxic stress, especially for *TP53*-null cells. **f,** Area under the curve (AUC) quantification. (Note that the drug induced cell death and doubling time could not be calculated.) Paired one-sided t-test, *TP53*-null *vs.* *TP53*-WT bortezomib in SFM p=0.18; *TP53*-null *vs.* *TP53*-WT bortezomib in ACM *,p=0.04; *TP53*-null bortezomib in ACM *vs.* *TP53*-null bortezomib in SFM *,p=0.04. n=6. BTZ, bortezomib. Boxplots: bar = median; box = 25–75th percentile; whiskers = range. See **Source Data**.

Supplementary Fig.9

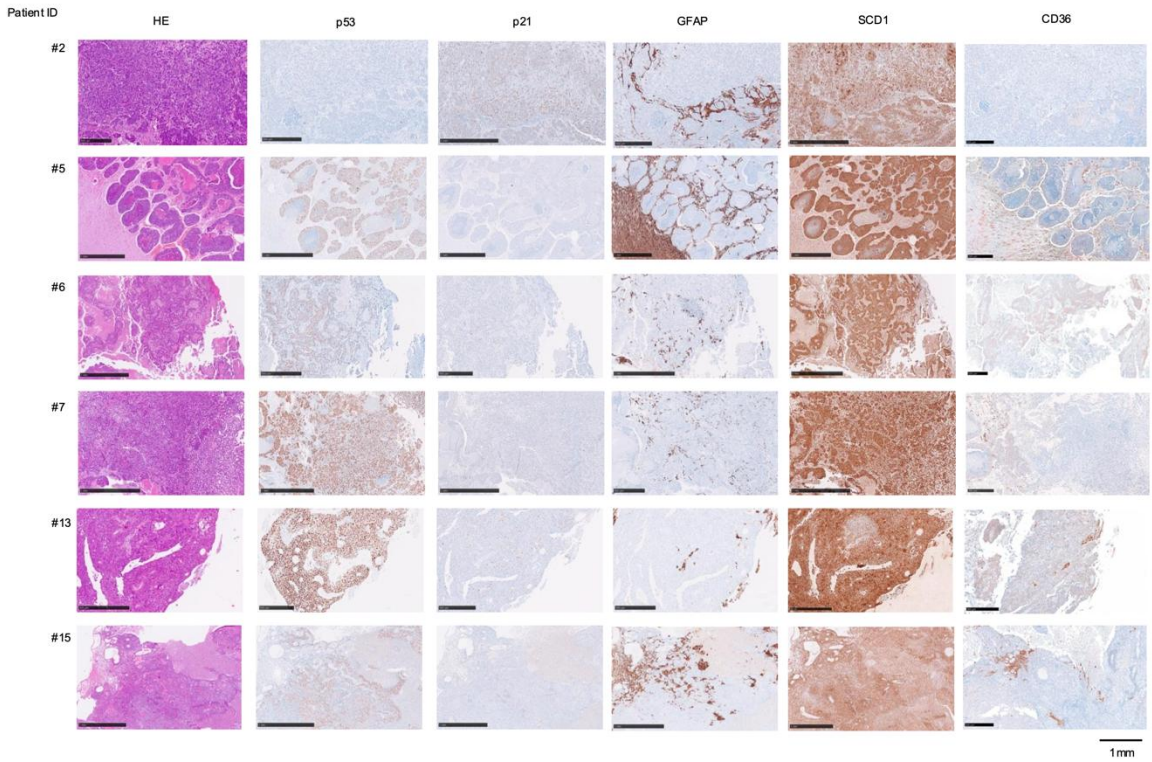

Supplementary Data Fig. 9: Human BCBMs exhibit low levels of p53 signaling, astrocyte tumor infiltration, and high levels of CD36 and SCD1 expression (related to Figures 3-5).

Representative images of BCBM sections from 6 patients, out of an analyzed cohort of 17 patient samples, are detailed in **Supplementary Table 6**. Sections were stained for haematoxylin-eosin (H&E) or with antibodies labeling p53, p21, GFAP, CD36 and SCD1 proteins. All sections showed very low or no detectable p21 staining, indicating a strong reduction or absence of p53 activity. Astrocyte infiltration could be detected in many tumors but the degree of infiltration was highly variable. CD36 staining was correlated with astrocyte infiltration. Strong SCD1 staining was detected across samples, consistent with upregulation of SCD1 protein levels in BCBM. For protein quantification in all samples, see **Supplementary Table 6**.

Supplementary Fig.10

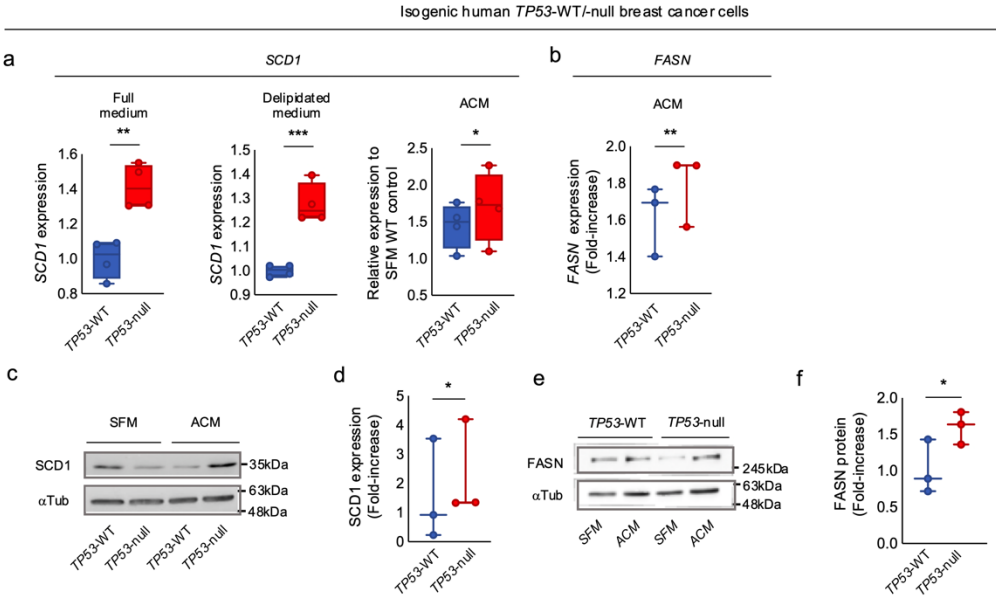

Supplementary Data Fig. 10: SCD1 and FAS are upregulated in *TP53*-null human BC cells and further stimulated by astrocyte conditioned medium (related to Fig. 5).

a, qPCR-based quantification of *SCD1* mRNA levels in *TP53*-WT and *TP53*-null human BC CAL51 cells cultured in full medium (left, one-sided t-test **,p=0.003), delipidated medium (center, one-sided t-test ***,$p=6*10^{-4}$) or ACM (right, one-sided t-test *,p=0.04). *SCD1* expression was significantly higher in *TP53*-null cells under all tested conditions. Full medium: n=4, delipidated medium: n=4, ACM: n=3. Boxplots: bar = median; box = 25–75th percentile; whiskers = range.

b, qPCR-based quantification of *FASN* mRNA levels in *TP53*-WT and *TP53*-null CAL51 cells cultured in ACM. *FASN* expression was significantly higher in the *TP53*-null cells. One-sided t-test, **,p=0.008. n=3. Bar, median; whiskers=range.

c, SCD1 protein quantification by Western blot in isogenic *TP53*-WT and *TP53*-null CAL51 cells cultured in SFM or ACM. ACM exposure significantly elevated SCD1 protein levels in *TP53*-null cells.

d, Quantification of SCD1 protein levels change in ACM *vs.* SFM. The effect of ACM on SCD1 protein expression was significantly stronger in *TP53*-null cells in comparison to *TP53*-WT cells. SCD1 protein levels are shown as fold-change of ACM over SFM conditions. Paired one-sided t-test, *p=0.03; *TP53*-WT: n=3, *TP53*-null: n=3. Bar, median; whiskers=range.

e, FASN protein quantification by Western blot in isogenic *TP53*-WT and *TP53*-null CAL51 cells cultured in SFM or ACM. ACM exposure significantly elevated FASN protein levels in *TP53*-null cells.

f, Quantification of FASN protein levels change in ACM *vs.* SFM. The effect of ACM on FASN protein expression was significantly stronger in *TP53*-null cells in comparison to *TP53*-WT cells. FASN protein levels are shown as fold-change of ACM over SFM conditions. Paired one-sided t-test, *,p=0.02; *TP53*-WT: n=3, *TP53*-null: n=3. Bar, median; whiskers=range. See **Source Data**.

Supplementary Fig.11

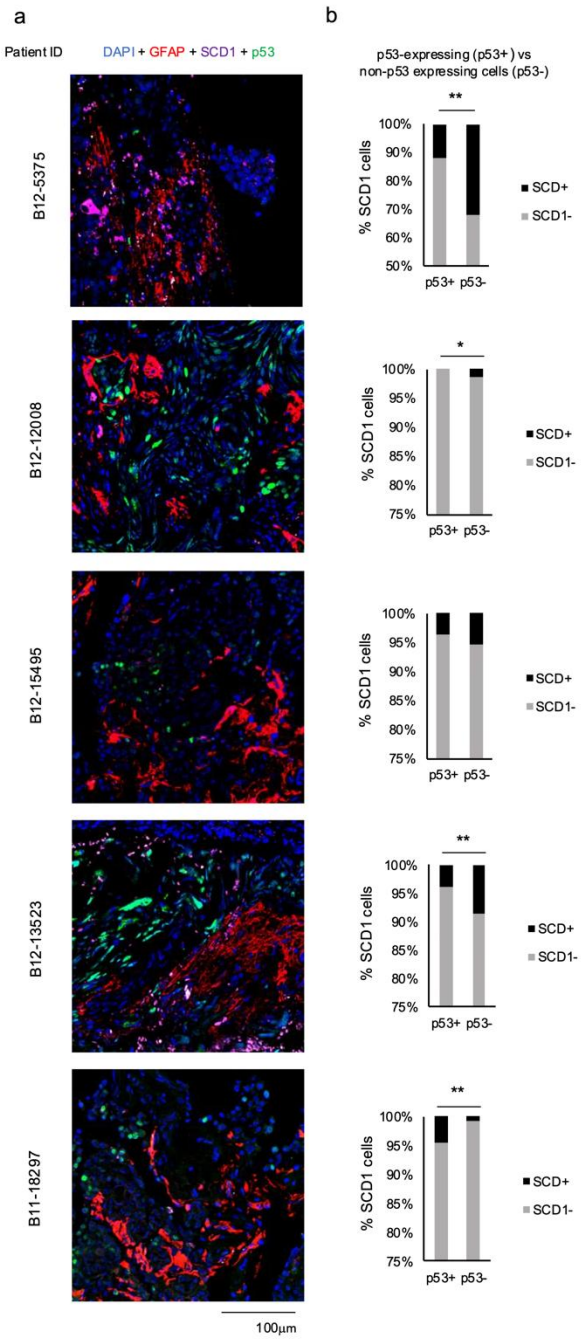

Supplementary Data Fig. 11: p*53* inactivation is associated with SCD1 protein expression in BCBM from human patients (related to Fig. 5).

a, Representative immunofluorescence images of human brain metastases from five BC patients, stained with antibodies against p53 (green), SCD1 (purple), and GFAP (red), as well as with DAPI nuclear staining (blue).

b, Comparison of the percentage of SCD1-positive cells between p53-expressing and non-p53-expressing tumor cells. p53-negative cells were significantly enriched for SCD1 expression in 4 out of 5 metastases. Two-sided Fisher's exact test, Patient ID: B12-5375 **p=0.004, B12-12008 *p=0.04, B12-15495 p=0.42, B12-13523 **,p=0.003, B11-18297 **,p=0.002. n=5. See **Source Data**.

Supplementary Fig.12

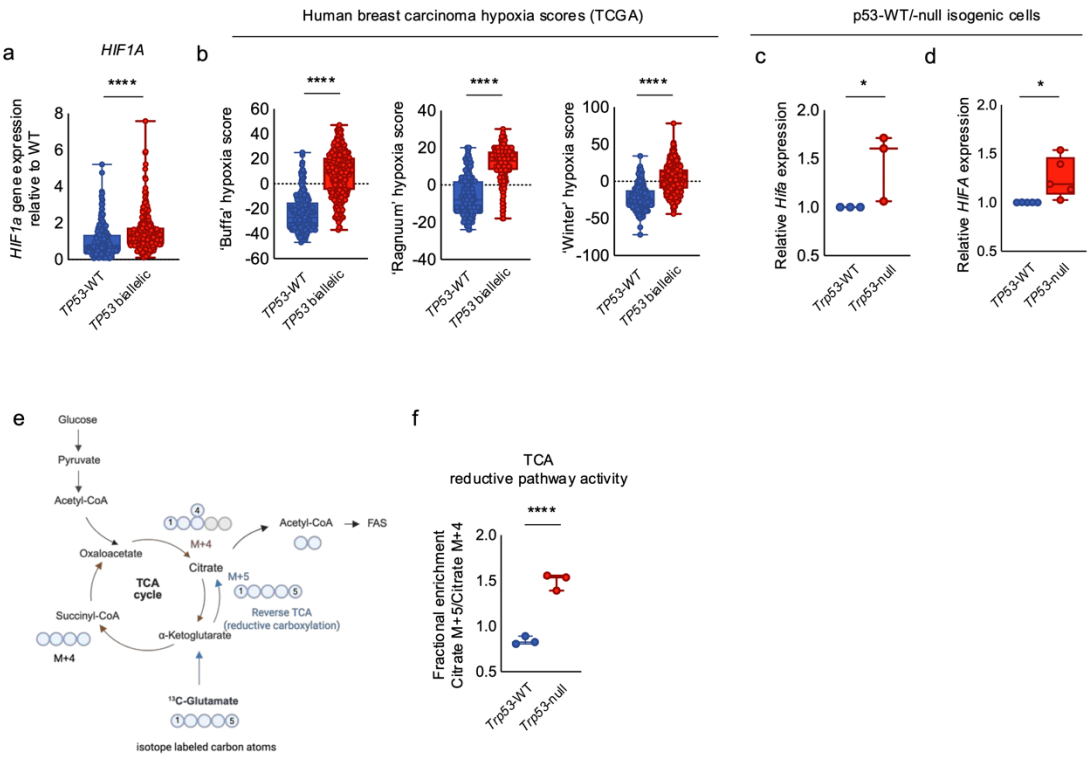

Supplementary Data Fig. 12: Metabolites secreted from astrocytes stimulate SCD1 expression and are incorporated into FAs (related to Fig. 5).

a, Comparison of *HIF1A* expression between tumors with *TP53*-WT and biallelic *TP53* perturbation in human primary BCs (TCGA). BCs with biallelic *TP53* perturbation exhibited increased levels of the hypoxia marker *HIF1A* in comparison to *TP53*-WT tumors. Two-sided t-test, ****,$p=1.4*10^{-9}$. Number of tumors: *TP53*-WT n=266, biallelic *TP53* inactivation n=279.

b, Comparison of three hypoxia scores between *TP53*-WT tumors and tumors with biallelic *TP53* inactivation in human primary BCs (TCGA). BCs with biallelic *TP53* perturbation had elevated levels of hypoxia scores in comparison to WT controls. 'Buffa' Hypoxia score[61]: biallelic *TP53* inactivation *vs.* *TP53*-WT ****,$p=7.6*10^{-81}$; 'Ragnum' hypoxia score: biallelic *TP53* inactivation *vs.* *TP53*-WT ****,$p=4.3*10^{-75}$: 'Winter' hypoxia score, biallelic *TP53* inactivation *vs.* *TP53*-WT ****,$p=1*10^{-50}$. Number of tumors: *TP53*-WT n=266, biallelic *TP53* inactivation n=279.

c, qPCR-based quantification of *Hif1a* expression in isogenic *Trp53*-WT and *Trp53*-null EMT6 cells. *Hif1a* mRNA levels are elevated in *Trp53*-null cells. Paired one-sided t-test, *,p=0.04, n=3.

d, qPCR-based quantification of *HIF1A* expression in isogenic *TP53*-WT and *TP53*-null CAL51 cells. *HIF1A* mRNA levels are elevated in *Trp53*-null cells. Paired one-sided t-test, *,p=0.02, n=5.

e, Schematic illustration of the metabolism of ^{13}C-glutamate through the oxidative pathway (TCA) to citrate (M+4) or, alternatively, through the reductive carboxylation (reverse TCA) of a-ketoglutarate to citrate (M+5). The citrate M+5/M+4 ratio is an indicator for relative pathway activity.

f, ^{13}C-glutamate tracing into citrate. Comparison of the citrate M+5/M+4 ratio in *Trp53*-WT and *Trp53*-null cells following 48hrs of incubation with ^{13}C-glutamate. Higher utilization of ^{13}C-glutamate in the reductive pathway was observed in *Trp53*-null *vs.* *Trp53*-WT cells. Two-sided t-test, ****,$p=5*10^{-5}$. n=3. Boxplots: bar = median; box = 25–75th percentile; whiskers = range. See **Source Data**. **Supplementary data Fig. 12e** created with BioRender.com.

Supplementary Fig.13

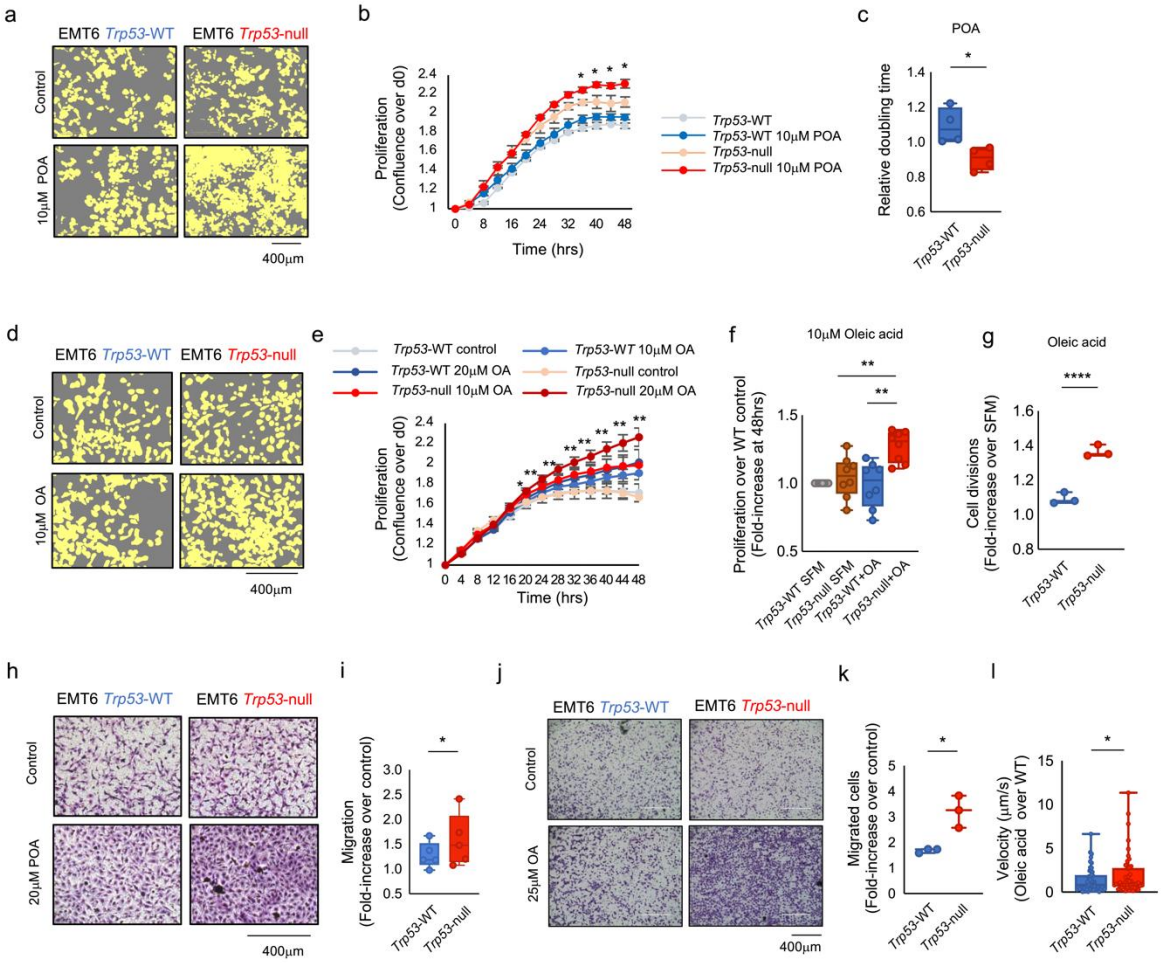

Supplementary Data Fig. 13: POA and OA supplementation phenocopies the effects of ACM on p53-null BC cell behaviour (related to Fig. 5).

a, Representative images of *Trp53*-WT and *Trp53*-null mouse BC EMT6 cells cultured with or without POA (10µM) for 48hrs.

b, Live imaging-based proliferation curves of *Trp53*-WT and *Trp53*-null mouse EMT6 cells cultured with or without POA (10µM) for 48hrs. Only *Trp53*-null cells showed a moderate increase in proliferation when POA was added to the culture medium. Two-sided t-test, *Trp53*-null *vs. Trp53*-null +POA 36hrs *,p=0.04, 40hrs *,p=0.03, 44hrs *,p=0.03, 48hrs *,p=0.04. Representative experiment; Control: n=2, treated: n=3. Error bars, mean +/- SEM.

c, Quantification of POA-stimulated proliferation at 48hrs. Shown as relative doubling time over control conditions. *Trp53*-null cells exposed to 10µM POA proliferated significantly better than *Trp53*-WT cells. POA treatment, *Trp53*-null *vs. Trp53*-WT, paired one-sided t-test *,p=0.03. Each datapoint represents an independent experiment n=4.

d, Representative images of *Trp53*-WT and *Trp53*-null EMT6 cells cultured with or without OA (10µM) for 48hrs.

e, Live imaging-based proliferation curves of *Trp53*-WT and *Trp53*-null EMT6 cells cultured with or without OA (10µM or 20µM) for 48hrs. Two-sided t-test, *Trp53*-null OA *vs. Trp53*-null +10/20µM OA, 20hrs p=0.08, *,p=0.02, 24hrs p=0.07, **,p=0.01, 28hrs *,p=0.04, **,p=0.006, 32hrs *,p=0.04, **,p=0.005, 36hrs *,p=0.04, **p=0.006, 40hrs *,p=0.04, **,p=0.006, 44hrs *,p=0.05, **,p=0.006, 48hrs *,p=0.05, **,p=0.006. n=3. Error bars, mean +/- SEM.

f, Quantification of OA-stimulated proliferation at 48hrs. Shown at fold-increase in cell number at 48hr. OA promoted the proliferation of *Trp53*-null cells more than that of *Trp53*-WT cells. Two-sided t-test *Trp53*-WT cells (1% FBS) *vs. Trp53*-WT cells (1% FBS +10µM OA) p=0.85; *Trp53*-null cells (1% FBS) *vs. Trp53*-null cells (1% FBS +10µM OA) p=0.004; *Trp53*-null cells (1% FBS +10µM OA) *vs. Trp53*-WT cells (1% FBS +10µM OA) relative to SFM controls **,p=0.001. *Trp53*-WT n=7, *Trp53*-null n=7.

g, Comparison of the effect of OA supplementation (10µM) on the growth of *Trp53*-WT and *Trp53*-null EMT6 cells. The proliferation-promoting effect of OA was significantly higher in *Trp53*-null cells in comparison to *Trp53*-WT cells. Shown as cell divisions in OA-supplemented medium over SFM. One-sided t-test, ***,$p=5*10^{-4}$. *Trp53*-WT: n=3, *Trp53*-null: n=3.

h, Transwell migration assay to assess the migration of EMT6 cells towards POA-containing medium. Representative images of *Trp53*-WT and *Trp53*-null EMT6 cells, stained in purple, showing their migration through the filter towards the lower chamber, which contained medium with or without POA (20µM).

i, Quantification of cell migration towards POA in the transwell assay at 20hrs. POA increased cell migration of both *Trp53*-WT and *Trp53*-null cells, but *Trp53*-null cells migrated significantly more towards POA than *Trp53*-WT control cells. Shown as fold-increase over respective medium controls. *Trp53*-null *vs*. *Trp53*-WT, one-sided t-test, *,p=0.04. n=5.

j, Transwell migration assay to assess the migration of EMT6 cells towards OA-containing medium. Representative images of *Trp53*-WT and *Trp53*-null EMT6 cells stained in purple, showing their migration through the filter towards the lower chamber, which contained medium with or without OA (25µM).

k, Quantification of cell migration towards OA in the transwell assay at 20hrs. OA increased cell migration of both *Trp53*-WT and *Trp53*-null cells, but its effect on *Trp53*-null cells was much stronger. Shown as the fold-increase over respective medium controls. Two-sided t-test, *,p=0.01. *Trp53*-WT: n=3, *Trp53*-null: n=3.

l, Live imaging-based quantification of the effect of OA on cell migration (velocity) of *Trp53*-WT and *Trp53*-null EMT6 cells. Cell velocity shown as fold-increase in OA over SFM. The effect of OA on cell velocity was significantly stronger in *Trp53*-null cells. One-sided paired t-test, *,p=0.045, n=48. Boxplots: bar = median; box = 25–75th percentile; whiskers = range. See **Source Data**.

Supplementary Fig.14

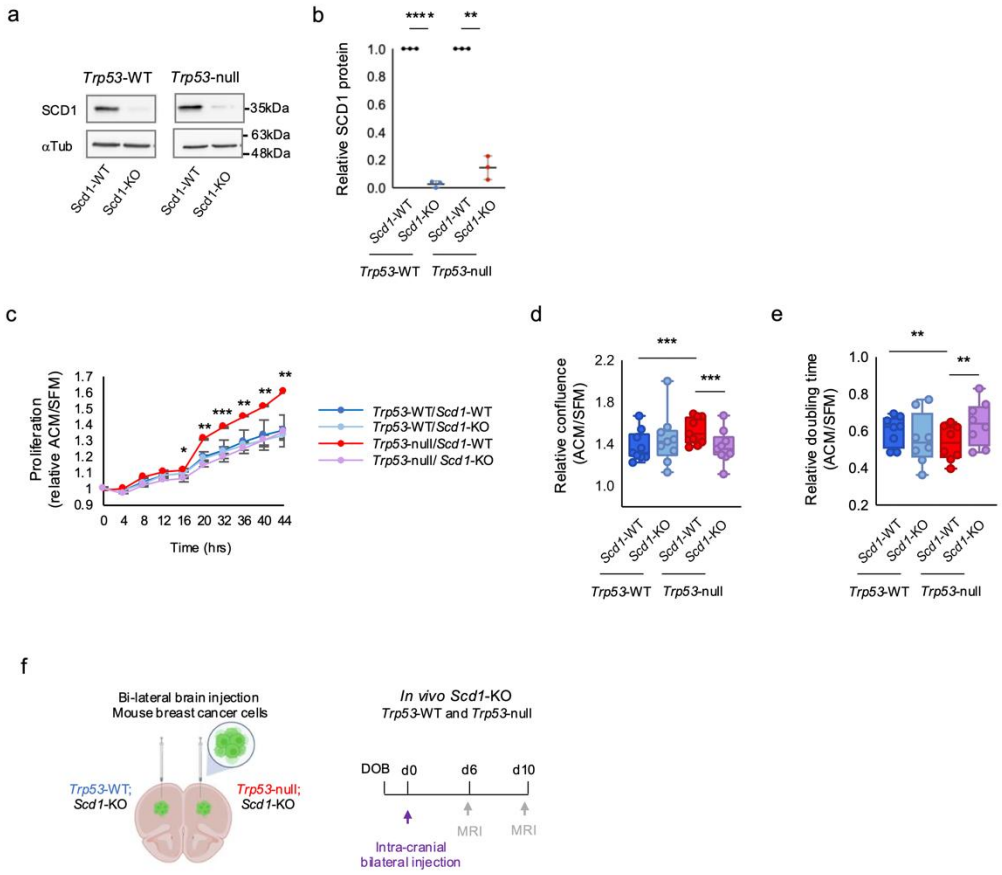

Supplementary Data Fig. 14: *Scd1* knockout reduces the p53-dependent effect of ACM on the proliferation of BC cells *in vitro* and *in vivo* (related to Fig. 5).

a, Validation of *Scd1* knockout in isogenic *Trp53*-WT and *Trp53*-null EMT6 cells. Western blot quantification shows abundant SCD1 protein in *Trp53*-WT and *Trp53*-null control cells, but a strong reduction in SCD1 protein levels in *Trp53*-WT and *Trp53*-null cells subjected to CRISPR/Cas9 gene editing using two gRNA guides targeting *Scd1*.

b, Western blot quantification. *Trp53*-WT and *Trp53*-null cells subjected to *Scd1* gene editing showed >85% reduction in SCD1 protein levels on the population level. Paired one-sided t-test *Trp53*-WT ****,$p=9.2*10^{-5}$, *Trp53*-null **,p=0.002. n=3. Error bars, mean +/-SD.

c, Live imaging-based proliferation of *Trp53*-WT and *Trp53*-null lacking SCD1 *(Trp53*-WT; *Scd1*-KO and *Trp53*-null; *Scd1*-KO) after ACM exposure, compared to their parental controls with functional SCD1. *Scd1*-KO reduced the ability of *Trp53*-null EMT6 cells to respond to ACM *in vitro*. One-sided t-test, *Trp53*-null;*Scd1*-WT *vs. Trp53*-null;*Scd1*-KO: 16hrs *,p=0.04, 20hrs **,p=0.004, 32hrs ***,p=0.001, 36hrs **,p=0.002, 40hrs **,p=0.002, 44hrs **,p=0.001. n=3. Error bars, mean +/- SEM.

d, Quantification of the effect of ACM on cell proliferation in *Trp53*-WT and *Trp53*-null EMT6 cells lacking the SCD1 protein. Shown as relative confluence in ACM over SFM at 40hrs. Knockout of *Scd1* did not affect the response of *Trp53*-WT cells to ACM, but significantly reduced the proliferation-promoting effect of ACM in *Trp53*-null cells. Paired one-sided t-test, *Trp53*-null *vs. Trp53*-WT ***,$p=2*10^{-4}$, *Trp53*-null;*Scd1*-KO *vs. Trp53*-null;*Scd1*-WT ***,p=0.001. n=8.

e, Quantification of the doubling times of *Trp53*-WT and *Trp53*-null EMT6 cells lacking SCD1 protein following stimulation with ACM for 48hrs. *Trp53*-null;*Scd1*-KO cells proliferated significantly less in response to ACM treatment than *Trp53*-null;*Scd1*-WT cells. Paired one-sided t-test, *Trp53*-null *vs. Trp53*-WT **,p=0.005, *Trp53*-null;*Scd1*-KO *vs. Trp53*-null;*Scd1*-WT **,p=0.006. n=8.

f, Schematic illustration of the experimental setup of bilateral intra-cranial injections of *Trp53*-WT and *Trp53*-null EMT6 cells with or without *Scd1* knockout. The timeline of the experiment is shown as well. Boxplots: bar = median; box = 25–75th percentile; whiskers = range. See **Source Data**. **Supplementary data Fig. 14f** created with BioRender.com.

Supplementary Fig.15

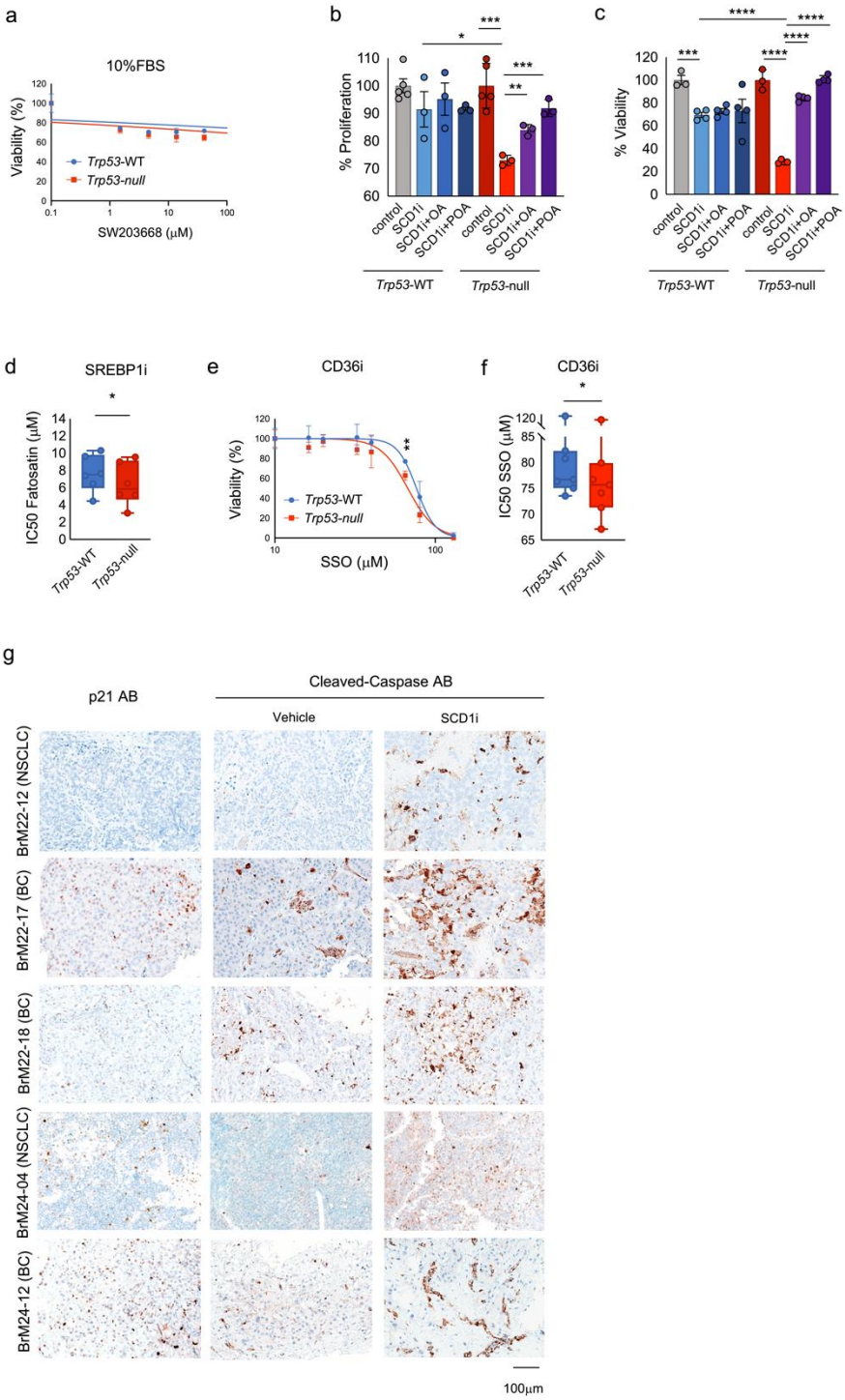

Supplementary Data Fig. 15: *p53* inactivation renders cells more sensitive to FAS inhibition (related to Fig. 7).

a, Comparison of the relative viability of *Trp53*-WT and *Trp53*-null EMT6 cells following 72hr exposure to SCD1 inhibition (SW203668) under high-lipid conditions (10% FBS). Both *Trp53*-WT and *Trp53*-null cells were insensitive to the drug when lipids were highly abundant in the cell culture medium. n=3. Error bars, mean +/- SEM.

b, Quantification of the proliferation rescue of SCD1i by OA and POA in *Trp53*-WT and *Trp53*-null EMT6 cells, evaluated 32hrs post FA supplementation. OA and POA supplementation (20µM) partially rescued the reduced proliferation following SCD1 inhibition (1µM) in *Trp53*-null EMT6 cells. One-sided t-test, SCD1 inhibition: *Trp53*-null *vs.* *Trp53*-WT *p=0.02, *Trp53*-null: SCD1 inhibition *vs.* SCD1 inhibition +OA **p=0.001, *Trp53*-null: SCD1 inhibition *vs.* SCD1 inhibition +POA ***,$p=1*10^{-4}$. n=4. Error bars, mean +/- SD.

c, Quantification of the viability rescue of SCD1i by OA and POA in *Trp53*-WT and *Trp53*-null EMT6 cells, evaluated by MTT 26hrs post FA supplementation. OA and POA (20µM) supplementation significantly rescued viability in EMT6 cells treated with the SCD1 inhibitor SW203668 (1µM). One-sided t-test, SCD1 inhibition: *Trp53*-WT ***,$p=4*10^{-4}$, *Trp53*-null ****,$p=1*10^{-6}$, *Trp53*-null *vs.* *Trp53*-WT, ****,$p=9*10^{-6}$, *Trp53*-null: SCD1 inhibition *vs.* SCD1 inhibition +OA ****,$p=1.1*10^{-8}$, *Trp53*-null: SCD1 inhibition *vs.* SCD1 inhibition +POA ****,$p=6.5*10^{-9}$. n=3. Error bars, mean +/- SD.

d, Comparison of the response to the SREBP1 inhibitor Fatostatin between *Trp53*-WT and *Trp53*-null EMT6 cells after 72hrs of treatment. Shown as IC50 values measured by MTT. *Trp53*-null cells are significantly more sensitive to the drug than *Trp53*-WT cells. Paired one-sided t-test, *,p=0.04, n=6.

e, Comparison of the relative viability of *Trp53*-WT and *Trp53*-null EMT6 cells treated for 72hrs with the CD36 inhibitor SSO. *Trp53*-null cells were significantly more sensitive to the drug. SSO inhibition (65µM) *Trp53*-WT *vs.* *Trp53*-null, one-sided t-test, **,p=0.004. Two-way ANOVA, SSO inhibition, *Trp53*-WT *vs.* *Trp53*-null ***,$p=1*10^{-4}$. n=3. Error bars, mean +/- SEM.

f, Comparison of the response to the CD36 inhibitor SSO between *Trp53*-WT and *Trp53*-null EMT6 cells after 72hrs of treatment. Shown as IC50 values measured by MTT. One-sided t-test, *,p=0.01, n=7.

g, Representative p21 and cleaved-caspase-3 antibody stainings of human patient-derived organotypic cultures treated with the SCD1 inhibitor SW203668 (3µM) or with vehicle control. All BM samples exhibited low to moderate p21 staining. SCD1i resulted in a marked increase in the fraction of apoptotic (cleaved-caspase-3-positve) cells. Boxplots: bar = median; box = 25–75th percentile; whiskers = range. See **Source Data**.

Supplementary Fig.16

a

Trp53-WT SFM

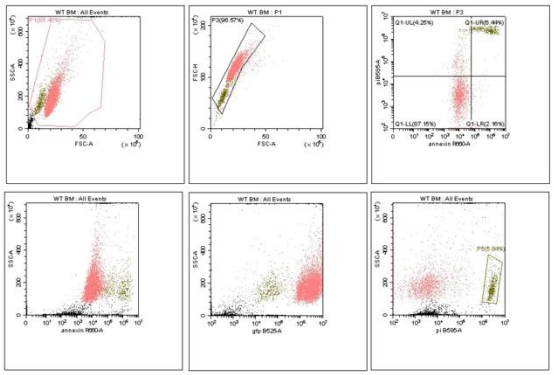

Trp53-null SFM

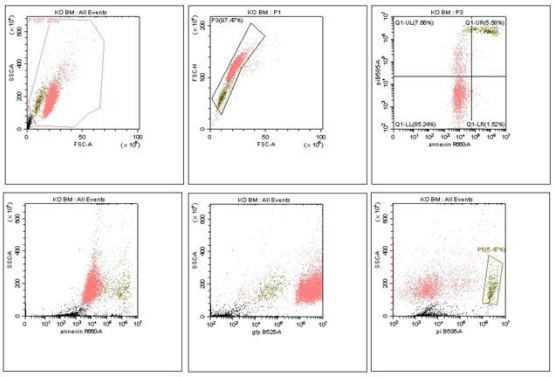

Trp53-WT ACM

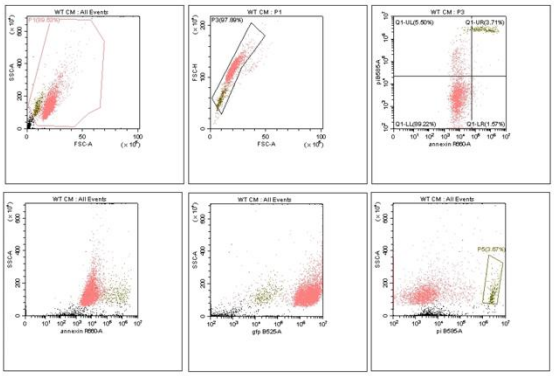

Trp53-null ACM

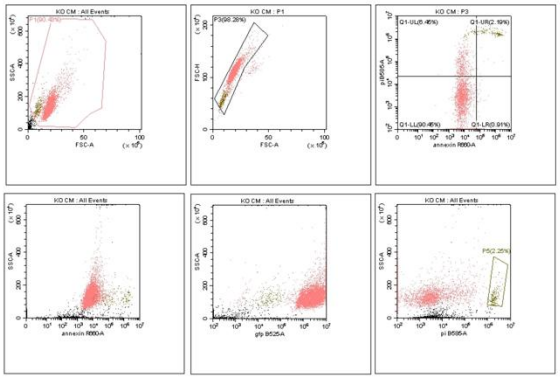

b

TP53-WT SFM

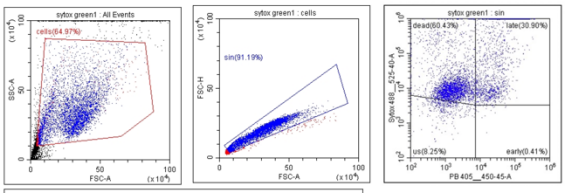

Tube Name: sytox green1
Sample ID:

Population	Events	% Total	% Parent
All Events	8139	100.00%	100.00%
cells	5288	64.97%	64.97%
sin	4822	59.25%	91.19%
late	1490	18.31%	30.90%
dead	2914	35.80%	60.43%
us	398	4.89%	8.25%
early	20	0.25%	0.41%

TP53-null SFM

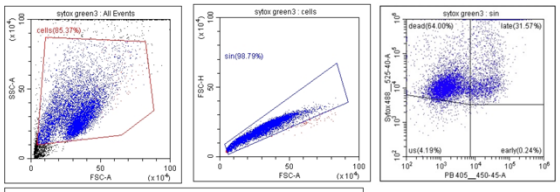

Tube Name: sytox green3
Sample ID:

Population	Events	% Total	% Parent
All Events	10000	100.00%	100.00%
cells	8537	85.37%	85.37%
sin	8434	84.34%	98.79%
late	2663	26.63%	31.57%
dead	5398	53.98%	64.00%
us	353	3.53%	4.19%
early	20	0.20%	0.24%

TP53-WT ACM

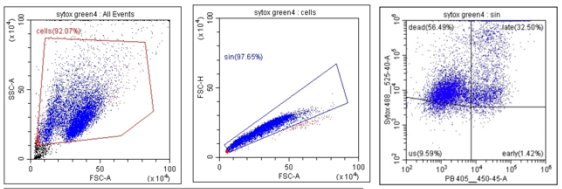

Tube Name: sytox green4
Sample ID:

Population	Events	% Total	% Parent
All Events	10000	100.00%	100.00%
cells	9207	92.07%	92.07%
sin	8991	89.91%	97.65%
late	2922	29.22%	32.50%
dead	5079	50.79%	56.49%
us	862	8.62%	9.59%
early	128	1.28%	1.42%

TP53-null ACM

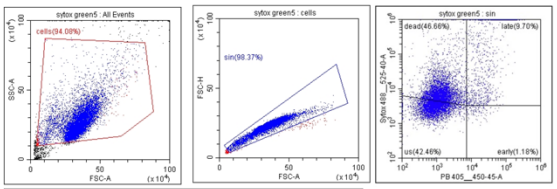

Tube Name: sytox green5
Sample ID:

Population	Events	% Total	% Parent
All Events	10000	100.00%	100.00%
cells	9408	94.08%	94.08%
sin	9255	92.55%	98.37%
late	898	8.98%	9.70%
dead	4318	43.18%	46.66%
us	3930	39.30%	42.46%
early	109	1.09%	1.18%

Supplementary Data Fig. 16: Flow cytometry analysis of BC cells (related to ED Fig. 5f and Supplementary Fig. 7k).

a, Flow cytometry gating of *Trp53*-WT and *Trp53*-null BC cells cultured with ACM and stained with AnnexinV. See **ED Fig. 5f. b,** Flow cytometry analysis of apoptosis in *TP53*-WT and *TP53*-null CAL51 cultured in ACM and stained with AnnexinV and Sytox green. See **Supplementary Fig.7k**.

Legends to Supplementary Tables

Supplementary Table 1: *TP53* status annotations for primary breast carcinoma in clinical datasets.

The status of chr17p copy number, *TP53* copy number, *TP53* mutation, and the resultant *TP53* status annotation for TCGA, METABRIC and MSK-IMPACT primary BCs.

Supplementary Table 2: GSEA of BMs compared to metastases in other organs (p53 signatures, 3 tabs).

Gene sets that are differentially expressed between BM and metastases in other organs. Unbiased GSEA and ssGSEA of the MSigDB 'Oncogenic' gene sets for 3 datasets: (**a**): GSE14017, (**b**): GSE14018, and (**c**): GSE245414. Highlighted in red are p53 signatures that indicate lower p53 activity in BM. Gene sets with $p<0.05$ are listed. Q-values for ssGSEA results were computed using the Benjamini–Hochberg method.

Supplementary Table 3: GSEA of primary breast tumors that would later metastasize to the brain *vs*. those that would metastasize to other organs (p53 signatures, 4 tabs).

a,b, Unbiased GSEA/ssGSEA comparing primary BC that would later metastasize to the brain *vs.* primary tumors that would later metastasize to other metastatic sites, shown for MBC (**a**) and GSE12276 (**b**).
c,d, GSEA of human BC cell lines (**c**), and of human carcinoma cell lines (**d**), comparing cell lines with high brain metastatic potential (top quartile) *vs.* those with low brain metastatic potential (bottom quartile). Highlighted in red are p53 signatures that indicate decreased p53 activity in tumors with high brain metastatic capacity. Q-values for ssGSEA results were computed using the Benjamini–Hochberg method.

Supplementary Table 4: ssGSEA analysis of *TP53*-null *vs. TP53*-WT tumors (BM signatures).

Unbiased ssGSEA of primary BCs with *vs.* without *TP53* alterations (*TP53* copy number loss or mutation). Shown are the top100 significant results, sorted by effect size, from the analysis of 3 independent data sets (METABRIC, TCGA, MBC). Brain metastasis/relapse signatures, indicating increased metastatic potential to the brain in *TP53*-null BC, are highlighted in red. Q-values for ssGSEA results were computed using the Benjamini–Hochberg method.

Supplementary Table 5: ssGSEA of primary breast tumors that would later metastasize to the brain *vs.* those that would metastasize to other organs (BM signatures, 2 tabs).

a, Unbiased ssGSEA of human primary BCs that would metastasize to the brain *vs.* those that would metastasize to other sites (GSE12276). **b**, Unbiased ssGSEA of human BC cell lines with high (top quartile) *vs.* low (bottom quartile) brain metastatic potential. The gene signatures 'Smid_breast_cancer_relapse_in_brain', 'Smid_breast_cancer_relapse_in_brain_up' and ' 'Smid_breast_cancer_relapse_in_brain_dn'

are highlighted in red. Q-values for ssGSEA results were computed using the Benjamini–Hochberg method.

Supplementary Table 6: IHC analysis of 17 BCBM clinical samples.

Assessment of p53, p21, SCD1 and GFAP immunostaining of BCBM clinical samples. For the experimental details, please see **Methods** section.

Supplementary Table 7: Comparison of GSEA signatures related to Adipogenesis, FA synthesis, FA uptake and FA activation, as presented in Fig. 4a-d and ED Fig. 6 a-d (8 tabs).

Shown are the following comparisons: **a,b**, Brain *vs.* other metastatic sites (GSE14017, GSE245414). **c,** BCs that metastasized to the brain *vs.* other metastatic sites (GSE12276). **d,e**, Primary BCs with *TP53* inactivation *vs. TP53*-WT tumors (METABRIC). **f**, Isogenic *TP53*-KO *vs. TP53*-WT CAL51 cells. **g**, BC cells with high *vs.* low metastatic potential. **h,** BM *vs.* corresponding primary BC. **i,** Brain *vs.* other metastatic sites, autopsy samples from the same patient.

Supplementary Table 8: GSEA of BM compared to metastases in other organs (Lipid metabolism signatures).

Unbiased GSEA comparing BCBM and metastases in other organs, for 3 datasets (GSE14017, GSE14018 and GSE245414) using the 'Reactome', 'Kegg' and 'GOMF' gene sets. Highlighted in red are signatures that indicate increased fatty acid biosynthesis and transport in BM. Q-values for ssGSEA results were computed using the Benjamini–Hochberg method.

Supplementary Table 9: GSEA and ssGSEA of BCBM *vs.* their matched primary tumors (Lipid metabolism signatures).

Unbiased GSEA and ssGSEA comparisons of primary BCs and their matched BMs focusing on the 'Reactome', 'GOBP' and 'GOMF' gene sets. Highlighted in red are signatures that indicate increased fatty acid biosynthesis and transport, as well as glutamate transport, in BM. Q-values for ssGSEA results were computed using the Benjamini–Hochberg method.

Supplementary Table 10: GSEA of BCs that would metastasize to the brain *vs.* those that would metastasize to other sites (Lipid metabolism signatures, 2 tabs).

a: Unbiased GSEA and ssGSEA comparing primary BCs that would metastasize to the brain vs. those that would metastasize to other organs (GSE12276) using 'Reactome' and 'GO' gene sets. **b**: Unbiased GSEA of human BC cell lines with high (top quartile) *vs.* low (bottom quartile) brain metastatic potential. Highlighted in red are FA biosynthesis and transport signatures elevated in BC cells with brain metastatic capacity. Q-values for ssGSEA results were computed using the Benjamini–Hochberg method.

Supplementary Table 11: ssGSEA of *TP53*-null *vs. TP53*-WT tumors (Lipid metabolism signatures).

Unbiased ssGSEA of primary BC with *vs.* without *TP53* alterations (*TP53* copy number loss or mutation). Shown are the 'Reactome', 'Kegg', 'GOBP' and 'GOMF' gene sets. Results are shown for two independent data sets (METABRIC, MBC). Highlighted in red are elevated FA biosynthesis signatures in BCs with *TP53* alterations.

Supplementary Table 12: ssGSEA of *TP53*-KO *vs. TP53*-WT CAL51 cells (Lipid metabolism signatures).

Unbiased ssGSEA of CAL51 BC cells subjected to knockout of *TP53* compared to their controls. Highlighted in red are FA biosynthesis and FA transport signatures that are elevated in *TP53*-KO cells. Q-values for ssGSEA results were computed using the Benjamini–Hochberg method.

Supplementary Table 13: Metabolic profiling of ACM by LC-MS.

Comparison of lipids and polar metabolites between ACM and SFM in triplicates. Shown as normalized data to internal standards and volume.

Supplementary Table 14: Gas chromatography-based analysis of FA content in *Trp53*-null and *Trp53*-WT EMT6 cells cultured in ACM.

Comparison of FA content in *Trp53*-null and *Trp53*-WT cells that were cultured for 20hrs in ACM or SFM. Data shown as mole %.

Supplementary Table 15: Isotope tracing experiments (4 tabs).

^{13}C-palmitic acid and ^{13}C-glutamic acid labeling of FAs in *Trp53*-WT and *Trp53*-null BC cells.

a, PA and POA isotope labeling following 1hrs incubation with ^{13}C-PA. **b**, PA and POA isotope labeling following 24hrs incubation with ^{13}C-PA. **c**, PA, SA and OA isotopologue distribution following 48hrs ^{13}C-glutamic incubation. **d**, Citrate isotope labeling following incubation with ^{13}C-glutamic acid for 48hrs.

Supplementary Table 16: p53 CUT&Tag in *TP53*-WT and *TP53*-null CAL51 cells.

List of p53-bound genomic sites in CAL51 breast cancer cells, their location, corresponding gene(s) and overlap with p53- and SREBP1-bound genes from the ChIP-atlas. Highlighted in red are p53-bound targets SREBF1 and SREBF2 (coding for SREBP1 and SREBP2), FASN and SCD1.

Supplementary Table 17: Gene expression consequences of DEPDC1 knockdown (2 tabs).

a, Unbiased GSEA comparing cells with *DEPDC1* knockdown to controls in the metastatic breast cancer cell line MDA-MB-231. **b,** ssGSEA comparing primary tumors from the TCGA breast cancer cohort with high (top 10%) *vs.* low (bottom 10%) mRNA levels of *DEPDC1*.

Supplementary Table 18: Comparison of gene essentiality (RNAi sensitivity) between *TP53*-null and *TP53*-WT human BC cell lines.

The top 500 differential RNAi sensitivities between *TP53*-null and *TP53*-WT BC cell lines (from DepMap[62]) were subjected to GSEA. Shown are the top 25 most significantly enriched pathways (MsigDB 'Hallmark' and C2 'Canonical Pathways' gene sets).

Supplementary Table 19: Reagents List (2 tabs).

Detailed information on reagents used in this study, including (**a**) CRISPR sgRNA sequences, siRNA sequences, primer sequences, and (**b**) antibodies and drugs.

Supplementary References

1. Powell, E., Piwnica-Worms, D. & Piwnica-Worms, H. Contribution of p53 to metastasis. *Cancer Discovery* vol. 4 405–414 (2014).
2. Zhang, X. H.-F. *et al.* Selection of bone metastasis seeds by mesenchymal signals in the primary tumor stroma. *Cell* **154**, 1060–1073 (2013).
3. Duchnowska, R. *et al.* Brain Metastasis Prediction by Transcriptomic Profiling in Triple-Negative Breast Cancer. *Clin Breast Cancer* **17**, e65–e75 (2017).
4. Zehir, A. *et al.* Mutational landscape of metastatic cancer revealed from prospective clinical sequencing of 10,000 patients. *Nat Med* **23**, 703–713 (2017).
5. Jin, X. *et al.* A metastasis map of human cancer cell lines. *Nature* **588**, 331–336 (2020).
6. Redman-Rivera, L. N. *et al.* Acquisition of aneuploidy drives mutant p53-associated gain-of-function phenotypes. *Nat Commun* **12**, 5184 (2021).
7. Priego, N. *et al.* STAT3 labels a subpopulation of reactive astrocytes required for brain metastasis article. *Nat Med* **24**, 1024–1035 (2018).
8. Doron, H. *et al.* Inflammatory Activation of Astrocytes Facilitates Melanoma Brain Tropism via the CXCL10-CXCR3 Signaling Axis. *Cell Rep* **28**, 1785-1798.e6 (2019).
9. Valiente, M. *et al.* The Evolving Landscape of Brain Metastasis. *Trends in Cancer* **4** 176–196 (2018).
10. Placone, A. L., Quiñones-Hinojosa, A. & Searson, P. C. The role of astrocytes in the progression of brain cancer: complicating the picture of the tumor microenvironment. *Tumor Biology* **37** 61–69 (2016).
11. Chen, Q. *et al.* Carcinoma–astrocyte gap junctions promote brain metastasis by cGAMP transfer. *Nature* **533**, 493–498 (2016).
12. Shumakovich, M. A. *et al.* Astrocytes from the brain microenvironment alter migration and morphology of metastatic breast cancer cells. *The FASEB Journal* **31**, 5049–5067 (2017).
13. Israeli Dangoor, S. *et al.* CCL2 blockade combined with PD-1/P-selectin immunomodulators impedes breast cancer brain metastasis. *Brain* **5**, 1740-1756 (2024).
14. Qu, F. *et al.* Crosstalk between small-cell lung cancer cells and astrocytes mimics brain development to promote brain metastasis. *Nat Cell Biol* **25**, 1506–1519 (2023).
15. Brose, S. A., Marquardt, A. L. & Golovko, M. Y. Fatty acid biosynthesis from glutamate and glutamine is specifically induced in neuronal cells under hypoxia. *J Neurochem* **129**, 400–412 (2014).
16. Munir, R., Lisec, J., Swinnen, J. V. & Zaidi, N. Lipid metabolism in cancer cells under metabolic stress. *Br J Cancer* **120**, 1090–1098 (2019).
17. Belfiore, F. & Iannello, S. Fatty Acid Synthesis from Glutamate in the Adipose Tissue of Normal Subjects and Obese Patients: An Enzyme Study. *Biochem Mol Med* **54**, 19–25 (1995).
18. Metallo, C. M. *et al.* Reductive glutamine metabolism by IDH1 mediates lipogenesis under hypoxia. *Nature* **481**, 380–384 (2012).
19. Natarajan, S. K. & Venneti, S. Glutamine Metabolism in Brain Tumors. Cancers (Basel). **11**:1628 (2019)
20. Zhang, C. *et al.* The Interplay Between Tumor Suppressor p53 and Hypoxia Signaling Pathways in Cancer. *Front Cell Dev Biol* **9**, 648808 (2021).
21. Tabor, D. E., Kim, J. B., Spiegelman, B. M. & Edwards, P. A. Identification of Conserved cis-Elements and Transcription Factors Required for Sterol-regulated Transcription of Stearoyl-CoA Desaturase 1 and 2. *Journal of Biological Chemistry* **274**, 20603–20610 (1999).
22. Yahagi, N. *et al.* p53 Activation in Adipocytes of Obese Mice. *Journal of Biological Chemistry* **278**, 25395–25400 (2003).

23. Harada, Y. *et al.* Cell-Permeable Peptide DEPDC1-ZNF224 Interferes with Transcriptional Repression and Oncogenicity in Bladder Cancer Cells. *Cancer Res* **70**, 5829–5839 (2010).
24. Kastenhuber, E. R. & Lowe, S. W. Putting p53 in Context. *Cell* vol. 170 1062–1078 (2017).
25. Nguyen, B. *et al.* Genomic characterization of metastatic patterns from prospective clinical sequencing of 25,000 patients. *Cell* **185**, 563-575.e11 (2022).
26. Schild, T., Low, V., Blenis, J. & Gomes, A. P. Unique Metabolic Adaptations Dictate Distal Organ-Specific Metastatic Colonization. *Cancer Cell* **33**, 347–354 (2018).
27. Altea-Manzano, P. *et al.* A palmitate-rich metastatic niche enables metastasis growth via p65 acetylation resulting in pro-metastatic NF-κB signaling. *Nat Cancer* **4**, 344–364 (2023).
28. Bergers, G. & Fendt, S.-M. The metabolism of cancer cells during metastasis. *Nat Rev Cancer* **21**, 162–180 (2021).
29. Li, F. & Simon, M. C. Cancer Cells Don't Live Alone: Metabolic Communication within Tumor Microenvironments. *Dev Cell* **54**, 183–195 (2020).
30. Feng, W. W., Zuppe, H. T. & Kurokawa, M. The Role of CD36 in Cancer Progression and Its Value as a Therapeutic Target. *Cells* **12**, 1605 (2023).
31. Feng, W. W. *et al.* CD36-Mediated Metabolic Rewiring of Breast Cancer Cells Promotes Resistance to HER2-Targeted Therapies. *Cell Rep* **29**, 3405-3420.e5 (2019).
32. Watt, M. J. *et al.* Suppressing fatty acid uptake has therapeutic effects in preclinical models of prostate cancer. *Sci Transl Med* **11**, (2019).
33. Rae, C., Fragkoulis, G. I. & Chalmers, A. J. Cytotoxicity and Radiosensitizing Activity of the Fatty Acid Synthase Inhibitor C75 Is Enhanced by Blocking Fatty Acid Uptake in Prostate Cancer Cells. *Adv Radiat Oncol* **5**, 994–1005 (2020).
34. Moon, S.-H. *et al.* p53 Represses the Mevalonate Pathway to Mediate Tumor Suppression. *Cell* **176**, 564-580.e19 (2019).
35. Bist, A., Fielding, C. J. & Fielding, P. E. p53 Regulates Caveolin Gene Transcription, Cell Cholesterol, and Growth by a Novel Mechanism. *Biochemistry* **39**, 1966–1972 (2000).
36. Laubach, K., Zhang, J. & Chen, X. The p53 Family: A Role in Lipid and Iron Metabolism. *Front Cell Dev Biol* **9**, (2021).
37. Zhang, Y. *et al.* The p53 Pathway in Glioblastoma. *Cancers (Basel)* **10**, 297 (2018).
38. Elahi, L. S. *et al.* Valproic acid targets IDH1 mutants through alteration of lipid metabolism. *npj Metabolic Health and Disease* **2**, 20 (2024).
39. Tanase, C. *et al.* Fatty Acids, CD36, Thrombospondin-1, and CD47 in Glioblastoma: Together and/or Separately? *Int J Mol Sci* **23**, 604 (2022).
40. Miska, J. & Chandel, N. S. Targeting fatty acid metabolism in glioblastoma. *Journal of Clinical Investigation* **133**, (2023).
41. Sheeter, D. A. *et al.* Unsaturated fatty acid synthesis is associated with poor prognosis in pediatric neuroblastoma and is differentially regulated by MYCN and tumor suppressor microRNAs. https://doi.org/10.1101/2023.04.20.537692
42. Eyme, K. M. *et al.* Targeting de novo lipid synthesis induces lipotoxicity and impairs DNA damage repair in glioblastoma mouse models. *Sci Transl Med* **15**, (2023).
43. Moskovits, N., Kalinkovich, A., Bar, J., Lapidot, T. & Oren, M. p53 Attenuates Cancer Cell Migration and Invasion through Repression of SDF-1/CXCL12 Expression in Stromal Fibroblasts. *Cancer Res* **66**, 10671–10676 (2006).
44. Mehta, S. A. *et al.* Negative regulation of chemokine receptor CXCR4 by tumor suppressor p53 in breast cancer cells: implications of p53 mutation or isoform expression on breast cancer cell invasion. *Oncogene* **26**, 3329–3337 (2007).
45. Pozzi, S. *et al.* MCP-1/CCR2 axis inhibition sensitizes the brain microenvironment against melanoma brain metastasis progression. *JCI Insight* **7**, (2022).
46. Shih, D. J. H. *et al.* Genomic characterization of human brain metastases identifies drivers of metastatic lung adenocarcinoma. *Nat Genet* **52**, 371–377 (2020).

47. Hsieh, H. H., Chen, Y. C., Jhan, J. R. & Lin, J. J. The serine protease inhibitor serpinB2 binds and stabilizes p21 in senescent cells. *J Cell Sci* **130**, 3272–3281 (2017).
48. Valiente, M. *et al.* Serpins promote cancer cell survival and vascular co-option in brain metastasis. *Cell* **156**, 1002–16 (2014).
49. Sossey-Alaoui, K., Pluskota, E., Szpak, D. & Plow, E. F. The Kindlin2-p53-SerpinB2 signaling axis is required for cellular senescence in breast cancer. *Cell Death Dis* **10**, (2019).
50. Feng, Z., Zhang, H., Levine, A. J. & Jin, S. The coordinate regulation of the p53 and mTOR pathways in cells. *Proceedings of the National Academy of Sciences* **102**, 8204–8209 (2005).
51. Cui, D. *et al.* The Cross Talk Between p53 and mTOR Pathways in Response to Physiological and Genotoxic Stresses. *Front Cell Dev Biol* **9**, (2021).
52. Budanov, A. V. & Karin, M. p53 Target Genes Sestrin1 and Sestrin2 Connect Genotoxic Stress and mTOR Signaling. *Cell* **134**, 451–460 (2008).
53. Akeno, N., Miller, A. L., Ma, X. & Wikenheiser-Brokamp, K. A. P53 suppresses carcinoma progression by inhibiting mTOR pathway activation. *Oncogene* **34**, 589–599 (2015).
54. Kwasnicki, A., Jeevan, D., Braun, A., Murali, R. & Jhanwar-Uniyal, M. Involvement of mTOR signaling pathways in regulating growth and dissemination of metastatic brain tumors via EMT. *Anticancer Res* **35**, 689–96 (2015).
55. Soliman, G. A. The integral role of mTOR in lipid metabolism. *Cell Cycle* **10**, 861–862 (2011).
56. Takahara, T., Amemiya, Y., Sugiyama, R., Maki, M. & Shibata, H. Amino acid-dependent control of mTORC1 signaling: a variety of regulatory modes. *J Biomed Sci* **27**, 87 (2020).
57. Swain, S. M., Shastry, M. & Hamilton, E. Targeting HER2-positive breast cancer: advances and future directions. *Nat Rev Drug Discov* **22**, 101–126 (2023).
58. Nasrazadani, A. & Brufsky, A. Neratinib: the emergence of a new player in the management of HER2+ breast cancer brain metastasis. *Future Oncology* **16**, 247–254 (2020).
59. Razavi, P. *et al.* The Genomic Landscape of Endocrine-Resistant Advanced Breast Cancers. *Cancer Cell* **34**, 427-438.e6 (2018).
60. Smid, M. *et al.* Subtypes of breast cancer show preferential site of relapse. *Cancer Res* **68**, 3108–14 (2008).
61. Aaltonen, L. A. *et al.* Pan-cancer analysis of whole genomes. *Nature* **578**, 82–93 (2020).
62. Arafeh, R., Shibue, T., Dempster, J. M., Hahn, W. C. & Vazquez, F. The present and future of the Cancer Dependency Map. *Nat Rev Cancer* **25**, 59–73 (2025).
63. Fast and accurate short read alignment with Burrows-Wheeler transform. *Bioinformatics*, Volume 25, Issue 14, 1754–1760 (2009),
64. The Sequence Alignment/Map format and SAMtools. *Bioinformatics*, Volume 25, Issue 16,, 2078–2079 (2009).
65. Liao, Y., Smyth, G. K. & Shi, W. featureCounts: an efficient general purpose program for assigning sequence reads to genomic features. *Bioinformatics* **30**, 923–30 (2014).
66. Robinson, M. D., McCarthy, D. J. & Smyth, G. K. edgeR: a Bioconductor package for differential expression analysis of digital gene expression data. *Bioinformatics* **26**, 139–140 (2010).
67. Korotkevich, G. *et al.* Fast gene set enrichment analysis. Preprint at https://doi.org/10.1101/060012 (2021).
68. Subramanian, A. *et al.* Gene set enrichment analysis: a knowledge-based approach for interpreting genome-wide expression profiles. *Proc Natl Acad Sci U S A* **102**, 15545–50 (2005).
69. Liberzon, A. *et al.* Molecular signatures database (MSigDB) 3.0. *Bioinformatics* **27**, 1739–1740 (2011).
70. Multi-omics analysis identifies RFX7 targets involved in tumor suppression and neuronal processes.

71. Liao, Y., Smyth, G. K. & Shi, W. The Subread aligner: fast, accurate and scalable read mapping by seed-and-vote. *Nucleic Acids Res* **41**, e108 (2013).
72. Ritchie, M. E. *et al.* limma powers differential expression analyses for RNA-sequencing and microarray studies. *Nucleic Acids Res* **43**, e47 (2015).
73. Law, C. W., Chen, Y., Shi, W. & Smyth, G. K. voom: Precision weights unlock linear model analysis tools for RNA-seq read counts. *Genome Biol* **15**, R29 (2014).
74. Leikin-Frenkel, A. *et al.* Blood fatty acid analysis reveals similar n-3 fatty acid composition in non-pregnant and pregnant women and their neonates in an Israeli pilot study. *Prostaglandins Leukot Essent Fatty Acids* **173**, 102339 (2021).
75. Millard, P. *et al.* IsoCor: isotope correction for high-resolution MS labeling experiments. *Bioinformatics* **35**, 4484–4487 (2019).
76. Bankhead, P. *et al.* QuPath: Open source software for digital pathology image analysis. *Sci Rep* **7**, 16878 (2017).

Source Data for Western blots

Supplementary Fig. 4e

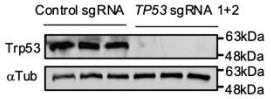

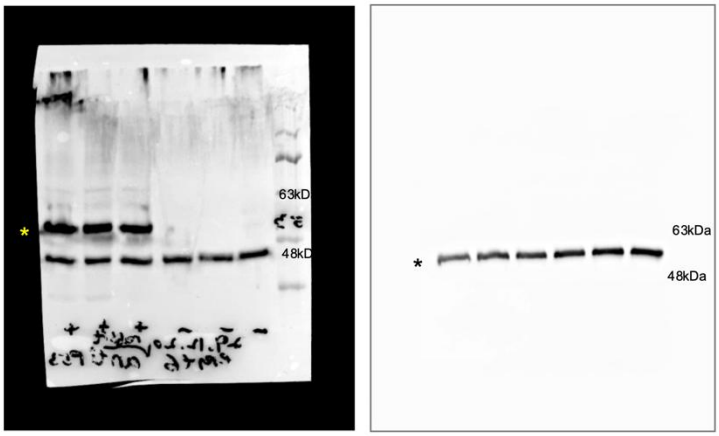

Supplementary Fig. 4h

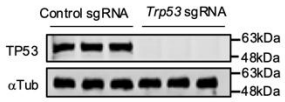

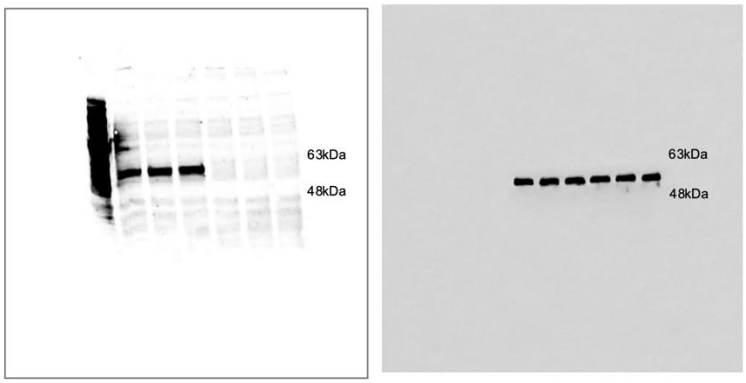

Supplementary Fig. 6i

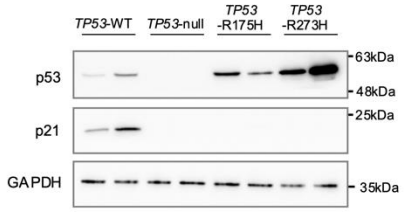

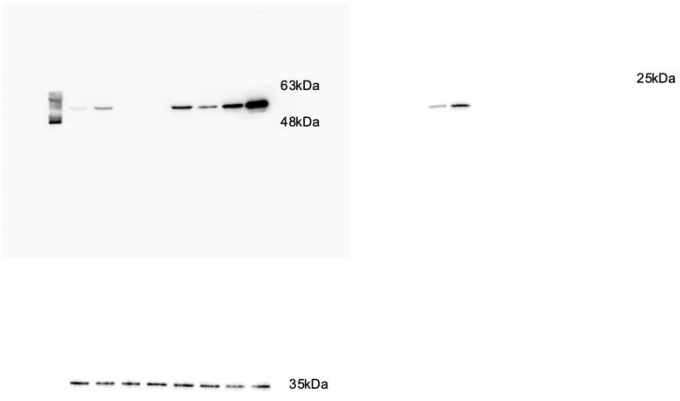

Supplementary Fig. 10c

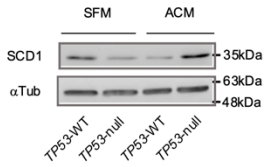

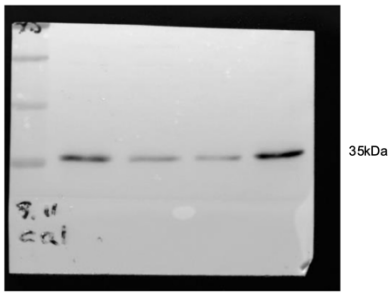

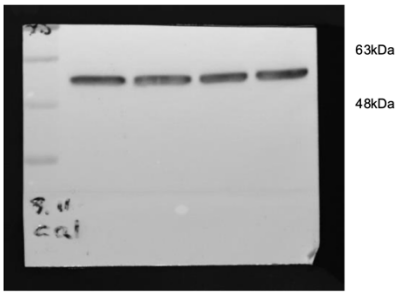

Supplementary Fig. 10e

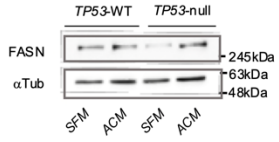

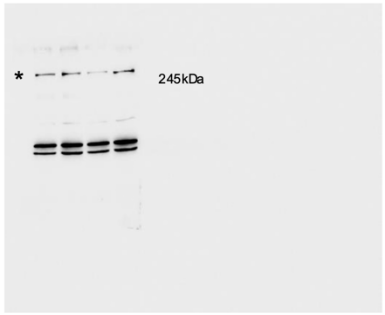

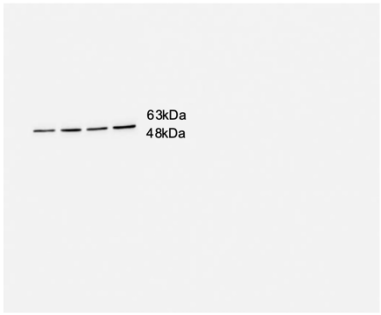

Supplementary Fig. 14a